May 2026

Supercooled First Order Phase Transitions and Gravitational Waves in a $B-L$-like Model

Lux Ruckstuhl

Theoretical Particle Physics
Department of Physics
Lund University

Bachelor thesis (15 hp) supervised by Roman Pasechnik

LUND
UNIVERSITY

Abstract

This thesis studies first-order phase-transition dynamics and the associated stochastic gravitational-wave background in classically conformal $B - L$-like extensions of the Standard Model. The scalar and gauge sectors are formulated at tree level and at one-loop order using a modified on-shell renormalization prescription designed to keep the vacuum structure fixed while allowing the tree-level flat-direction scalar to acquire a loop-induced mass. The finite-temperature effective potential is then used to analyse supercooled first-order phase transitions and the resulting gravitational-wave spectra. Numerical benchmark studies are performed with the Python package `TransitionSolver`. For the limited benchmark points considered here, the predicted gravitational-wave signals are below the projected detectability of LISA and current pulsar-timing-array searches. These results should therefore be interpreted as an exploratory benchmark analysis rather than as a general exclusion of the model class.

Popular description

The Standard Model is the central theoretical framework of particle physics. It describes the fundamental particles that give rise to all known matter in the universe; quarks that give rise to baryons like protons and neutrons, leptons such as the electron, and bosons such as the photon or the Higgs boson. Crucially, it has always been known to be limited, lacking explanations for dark matter, gravity and more. This was felt in September 2015, when a gravitational wave passed through the earth, measured by the gravitational wave measurement experiment LIGO [1]. Waves of gravitational radiation, known as gravitational waves, have been theorised, derived from Einstein's equation of general relativity [2], yet it took one hundred years to finally measure one, resulting in the Nobel Prize in physics in 2017. Predictably, fervour for research into gravitational waves skyrocketed, resulting eventually in this thesis.
The gravitational waves detected at LIGO were the result of two black holes merging; however, this is not the only possible origin of gravitational waves. In the early universe, the plasma filling the universe was in an excited state. As the universe expanded and cooled, the plasma began to transition, from the excited state, to the true vacuum of the universe known to us.

This thesis investigates an extension to the Standard Model of particle physics by an extra force and an extra Higgs-like boson. In the Standard Model, electromagnetic charge conservation gives rise to the (gauge) boson governing electromagnetic interactions, the photon. Analogously, the extra force introduced causes the conservation of the difference between baryon (B) and lepton (L) numbers, $B - L$ is conserved in any interaction of this model, giving rise to a new gauge boson. The $B - L$ model is widely studied, both due to its simplicity, and due to its wide range of applicability, giving an explanation for dark matter [3, 4], the matter anti-matter asymmetry in the universe [5, 6], and gravitational waves from the early universe [7, 8].
The plasma's transition from the excited, false vacuum, to the true vacuum, happens spontaneously, and is dictated by the Higgs and $B - L$ contributions. The transition occurs, leaving behind bubbles of the true vacuum, which rapidly expand, until the universe is entirely filled with true vacuum, as we know it today. This rapid motion of the bubbles through the plasma, and collisions of bubbles with each other, results in large amounts of energy being released, in the form of gravitational waves [9, 10]. These gravitational waves, arising from the predictions of the $B - L$ model, are numerically calculated, and then compared to the data of gravitational wave discoveries [11–14], and the measurement range of the planned gravitational wave detector LISA [15, 16]. If a gravitational wave signal with compatible properties were detected in the future, it could provide important evidence for physics beyond the Standard Model and help constrain models of this type. However, such a signal would not by itself uniquely confirm the model, since different models can lead to similar gravitational wave spectra.

Contents

List of acronyms

SM	Standard Model
OS	On-Shell
VEV	Vacuum Expectation Value
RHN	Right-Handed Neutrino
FOPT	First-Order Phase Transition
GW	Gravitational Wave
SGWB	Stochastic Gravitational-Wave Background
MHD	Magnetohydrodynamic
LIGO	Laser Interferometer Gravitational-Wave Observatory
LISA	Laser Interferometer Space Antenna
NANOGrav	North American Nanohertz Observatory for Gravitational Waves
PTA	Pulsar Timing Array
PPTA	Parkes Pulsar Timing Array
EPTA	European Pulsar Timing Array

List of Figures

List of Tables

1 Introduction

The Standard Model (SM) of particle physics has undoubtedly been extremely successful since its introduction. It accurately describes the electroweak and strong forces, predicted the Higgs boson and much more [17]. Nonetheless, it is limited; it lacks explanations for gravity, dark matter, baryon asymmetry, and the hierarchy problem [18]. Countless new theories have been proposed to remedy some or all of these issues, such as supersymmetry, string theory and many others. In this thesis, the focus will be on a simple $U'(1)$ extension of the Standard Model. The extension discussed is a classically conformal model which introduces a new gauge symmetry, baryon minus lepton number ($B-L$), with the introduction of three generations of right-handed neutrinos (ν_R), required for anomaly cancellation, and a complex Higgs singlet S that breaks the new gauge symmetry [19, 20]. In the full $B-L$ framework, the right-handed neutrinos can participate in neutrino-mass generation through a seesaw mechanism and, in suitable variants, may also be connected to dark-matter phenomenology [3, 4, 21, 22]. In the simplified setup analysed below, however, the right-handed-neutrino Yukawa couplings are neglected, so the focus is on the scalar and gauge sectors and its phase-transition dynamics. The breaking of the $B-L$ gauge symmetry gives mass to the new Z' gauge boson. In the most general Abelian sector, the new gauge field may mix with the hypercharge gauge field, although this mixing is neglected in the simplified analysis. The effective potential, a real scalar function, that is constructed from the classical scalar fields, is used to determine when the symmetry is spontaneously broken. Furthermore, the $B-L$ model has often been considered a potential explanation for the stochastic gravitational wave background (SGWB) [7, 8, 23, 24].

Cosmological First Order Phase Transitions (FOPT) describe the rapid transition of the plasma in the early universe from a local minimum, the false vacuum, to the global minimum, the true vacuum. The FOPT causes the nucleation and expansion of bubbles of true vacuum. The three main sources of gravitational waves (GWs) from the early universe are: bubble collisions, sound waves, and turbulence [2, 8–10]. As gravitational waves are not absorbed, and are only affected by the expansion of the universe, which redshifts the waves, they provide a lot of information about processes in the very early universe, the sources of which have long since disappeared. The detection of gravitational waves has been a growing area of focus since the detection of gravitational waves at the LIGO experiment in 2015 [1], leading to the development of new tools to investigate GWs. The SGWB can be searched with the planned LISA instrument [15, 16], and compared to NANOGrav [12] and other pulsar timing array (PTA) data to constrain or motivate regions of the model parameter space [10, 11, 25].

This thesis is structured as follows: In the first section, Section 2, the modified $B-L$ model used is described analytically, and the masses of the gauge and scalar bosons are derived, first at tree-level, then at one-loop level for zero-temperature, where a modified on-shell (OS) scheme is implemented. Finally thermal contributions are included, both finite temperature contributions and summing over leading infrared-divergent terms, in a process called Daisy resummation, via a method called the Arnold-Espinosa Method [26]. The next section, Section 3, describes the fundamental dynamics of FOPT and of the thermodynamic parameters. Then the focus is set on supercooled FOPT specifically, and the mechanisms of gravitational wave production are described. Finally, the implementation of the model, obtained from the python module `TransitionSolver` [27–29], is described. The numerical results obtained from `TransitionSolver` are evaluated in Section 4. The findings are summarised and concluded in the final section, Section 5, with any relevant additional material to be found in the Appendix.

2 Model description

2.1 $B - L$ Model

The model discussed is a classically conformal extension of the Standard Model by a $U'(1)_{B-L}$ gauge group that governs the $B - L$ symmetry, such that our model can be written as a combination of gauge groups $SU(3)_c \times SU(2)_L \times U(1)_Y \times U'(1)_{B-L}$. The particle content consists of the SM fields, three generations of right-handed neutrinos (RHNs), a complex scalar singlet S with $B - L$ charge $x_S = +2$, and the corresponding massive gauge boson Z' after spontaneous $B - L$ breaking. In the full minimal $B - L$ model, the Yukawa interaction $S\overline{\nu_R^c}\nu_R$ gives Majorana masses to the RHNs after S obtains a vacuum expectation value [8]. In the simplified analytical setup used here, these Yukawa couplings are set to zero, so the RHNs are retained for anomaly cancellation but do not contribute to the effective potential. The particles and their charges under each gauge group are listed in Table 1 below, adapted from Ref. [20].

Field	$SU(3)_c$	$SU(2)_L$	$U(1)_Y$	$U'(1)_{B-L}$
q_L	**3**	**2**	$\frac{1}{6}$	$\frac{1}{3}$
u_R	**3**	**1**	$\frac{2}{3}$	$\frac{1}{3}$
d_R	**3**	**1**	$-\frac{1}{3}$	$\frac{1}{3}$
ℓ_L	**1**	**2**	$-\frac{1}{2}$	-1
e_R	**1**	**1**	-1	-1
ν_R	**1**	**1**	0	-1
$\mathcal{H}$	**1**	**2**	$\frac{1}{2}$	0
S	**1**	**1**	0	2

Table 1: Particles and their charges in the $SM \times U'(1)_{B-L}$ model, including the singlet S, and three right-handed neutrinos required for anomaly cancellation.

The model is verified to be gauge and gravitational anomaly-free by checking it against the conditions presented in [19], with the calculations shown explicitly in Appendix A. The scalar field charges do not enter the anomaly sums, as only chiral fermions contribute to the gauge and mixed gravitational anomalies. The scalar fields are included in Table 1 for completeness, and due to their contribution to the gauge boson masses.

2.2 Gauge boson mass

The covariant derivative is defined as:

$$D_\mu = \partial_\mu - ig_1 Y B_\mu - ig_2 \frac{\sigma_a}{2} A^a_\mu - ig_3 \frac{\lambda_\alpha}{2} G^\alpha_\mu - ig_{12} x B_\mu - ig_{21} Y B'_\mu - ig_{B-L} x B'_\mu. \tag{2.1}$$

Here Y denotes the usual SM hypercharge, with $Q = T_3 + Y$, σ_a and λ_α are the Pauli and Gell-Mann matrices respectively, and x denotes the $B-L$ charge. The parameters g_{12} and g_{21} describe the kinetic mixing between $U(1)_Y$ and $U'(1)_{B-L}$ after the Abelian kinetic terms have been diagonalized. In the simplified analysis below these mixing effects are neglected, as they are constraint to be very small [30]. The remaining parameters g_1, g_2, g_3 and g_{B-L} are the gauge couplings of $U(1)_Y, SU(2)_L, SU(3)_c$ and $U'(1)_{B-L}$, respectively. Furthermore, the Higgs and S scalars are defined as

$$\mathcal{H} = \frac{1}{\sqrt{2}} \begin{pmatrix} \omega_1 + i\omega_2 \\ \phi_h + h_r + ia_h \end{pmatrix}, \quad S = \frac{1}{\sqrt{2}}(\phi_\sigma + h'_r + ia_\sigma). \tag{2.2}$$

The fields ϕ_h and ϕ_σ constitute the background fields, while h_r, h'_r are quantum excitations about the minima, and ω_1, ω_2, a_h, and a_σ give rise to the Goldstone bosons $G_\pm, G_1$, and G_2

respectively. Around the broken vacuum, $G_\pm$ and G_1 are associated with the electroweak gauge bosons, while G_2 is associated with the broken $U(1)_{B-L}$ symmetry and is absorbed by the Z'.
From this the Hessian $\mathbf{M_V}^2$ is found by expanding $|D_\mu \mathcal{H}|^2$ and $|D_\mu S|^2$, which in the basis $\{A^1_\mu, A^2_\mu, B_\mu, A^3_\mu, B'_\mu\} \otimes \{A^1_\mu, A^2_\mu, B_\mu, A^3_\mu, B'_\mu\}$ is

$$\mathbf{M_V}^2 = \begin{pmatrix} \frac{g_2^2\phi_h^2}{4} & 0 & 0 & 0 & 0 \\ 0 & \frac{g_2^2\phi_h^2}{4} & 0 & 0 & 0 \\ 0 & 0 & \frac{g_1^2\phi_h^2}{4} & -\frac{g_1 g_2\phi_h^2}{4} & \frac{g_1 g_{12}\phi_h^2}{4} \\ 0 & 0 & -\frac{g_1 g_2\phi_h^2}{4} & \frac{g_2^2\phi_h^2}{4} & -\frac{g_2 g_{12}\phi_h^2}{4} \\ 0 & 0 & \frac{g_1 g_{12}\phi_h^2}{4} & -\frac{g_2 g_{12}\phi_h^2}{4} & -\frac{g_{12}^2\phi_h^2}{4} + 4g_{B-L}^2\phi_\sigma^2 \end{pmatrix}. \tag{2.3}$$

For the rest of this paper, g_{12} is set to zero, as it is experimentally constraint to be very small [30]. The eigenvalues of $\mathbf{M_V}^2$ provide the field-dependent masses of the gauge bosons. $M_\gamma^2 = 0, \quad M_{W^\pm}^2 = \frac{g_2^2\phi_h^2}{4}, \quad M_{Z^0}^2 = \frac{(g_1^2+g_2^2)\phi_h^2}{4}, \quad M_{Z'}^2 = 4g_{B-L}^2\phi_\sigma^2.$

2.3 Effective Potential

The effective potential plays a crucial role in this analysis as it causes the phase transition discussed later on. The scalar singlet S causes $U(1)_{B-L}$ symmetry breaking via its vacuum expectation value. In a classically conformal Gildener–Weinberg-type setup, the tree-level potential contains a flat radial direction. The corresponding massless scalar is the "scalon" σ, the pseudo-Goldstone boson associated with spontaneously broken classical scale invariance. In the limit $v_\sigma \gg v_h$, where v_h and v_σ are the vacuum expectation values (VEVs) for the Higgs and σ bosons, this state is mostly singlet-like and acquires a mass through loop corrections.

2.3.1 Tree-Level Potential

The simplified $B - L$ model discussed is a classically conformal model, as the tree-level potential contains only quartic terms. The tree-level potential is given by the scalar part of the Lagrangian, as $\mathcal{L}_{\text{scalar}} = T - V_{\text{tree}}$, with T containing the kinetic terms.

$$V_{\text{tree}} = \lambda_h[\mathcal{H}^\dagger\mathcal{H}]^2 + \lambda_\sigma[S^*S]^2 + \lambda_{h\sigma}[\mathcal{H}^\dagger\mathcal{H} \cdot S^*S]. \tag{2.4}$$

Equation 2.4 is expanded with the expressions for $\mathcal{H}$ and S, given in Equation 2.2. The tree-level potential is then analysed, and a Hessian matrix is calculated in basis $\{\omega_1, \omega_2, h_r, h'_r, a_h, a_\sigma\} \otimes \{\omega_1, \omega_2, h_r, h'_r, a_h, a_\sigma\}$.

$$
\mathbf{M_s}^2 = \begin{pmatrix}
\lambda_h\phi_h^2 + \frac{\lambda_{h\sigma}\phi_\sigma^2}{2} & 0 & 0 & 0 & 0 & 0 \\
0 & \lambda_h\phi_h^2 + \frac{\lambda_{h\sigma}\phi_\sigma^2}{2} & 0 & 0 & 0 & 0 \\
0 & 0 & 3\lambda_h\phi_h^2 + \frac{\lambda_{h\sigma}\phi_\sigma^2}{2} & \lambda_{h\sigma}\phi_h\phi_\sigma & 0 & 0 \\
0 & 0 & \lambda_{h\sigma}\phi_h\phi_\sigma & 3\lambda_\sigma\phi_\sigma^2 + \frac{\lambda_{h\sigma}\phi_h^2}{2} & 0 & 0 \\
0 & 0 & 0 & 0 & \lambda_h\phi_h^2 + \frac{\lambda_{h\sigma}\phi_\sigma^2}{2} & 0 \\
0 & 0 & 0 & 0 & 0 & \lambda_\sigma\phi_\sigma^2 + \frac{\lambda_{h\sigma}\phi_h^2}{2}
\end{pmatrix}. \tag{2.5}
$$

When diagonalised, we obtain the field-dependent masses, with notation following [8], $M_h^2 = \frac{1}{4}(6\lambda_h\phi_h^2 + \lambda_{h\sigma}\phi_h^2 + \lambda_{h\sigma}\phi_\sigma^2 + 6\lambda_\sigma\phi_\sigma^2 - \Delta)$,

$M_\sigma^2 = \frac{1}{4}(6\lambda_h\phi_h^2 + \lambda_{h\sigma}\phi_h^2 + \lambda_{h\sigma}\phi_\sigma^2 + 6\lambda_\sigma\phi_\sigma^2 + \Delta)$,

$\Delta = \sqrt{(-6\lambda_h\phi_h^2 - \lambda_{h\sigma}\phi_h^2 - \lambda_{h\sigma}\phi_\sigma^2 - 6\lambda_\sigma\phi_\sigma^2)^2 - 4(6\lambda_h\lambda_{h\sigma}\phi_h^4 + 36\lambda_h\lambda_\sigma\phi_h^2\phi_\sigma^2 - 3\lambda_{h\sigma}^2\phi_h^2\phi_\sigma^2 + 6\lambda_{h\sigma}\lambda_\sigma\phi_\sigma^4)}$,

$M_{G_1}^2 = \lambda_h\phi_h^2 + \frac{\lambda_{h\sigma}\phi_\sigma^2}{2}, \quad M_{G_2}^2 = \lambda_\sigma\phi_\sigma^2 + \frac{\lambda_{h\sigma}\phi_h^2}{2}, \quad M_{G_\pm}^2 = \lambda_h\phi_h^2 + \frac{\lambda_{h\sigma}\phi_\sigma^2}{2}.$

At tree-level minimum, the mass matrix $\mathbf{M_s}^2$ has one massive eigenstate, which we associate with the observed Higgs boson, and five massless eigenstates. One is the massless flat-direction state of the "scalon" we identify as σ [31], the remaining massless modes are gauge Goldstone modes. The σ is not associated with a gauge boson, rather it obtains a physical mass through one-loop level corrections.
Imposing the conditions

$$
\left.\frac{dV_{\text{tree}}}{d\psi_i}\right|_{\phi_h=v_h,\phi_\sigma=v_\sigma} = 0, \tag{2.6}
$$

at $(\phi_h, \phi_\sigma) = (v_h, v_\sigma)$, which are known as the tadpole conditions at tree-level. Together with the requirements that $\mathbf{M_s^2}$ has massive eigenstate M_h^2, and massless Goldstone and flat-direction states at tree-level, these conditions determine the quartic couplings.

$$
\lambda_h = \frac{M_h^2 v_\sigma^2}{2v_h^2(v_h^2+v_\sigma^2)}, \quad \lambda_\sigma = \frac{M_h^2 v_h^2}{2v_\sigma^2(v_h^2+v_\sigma^2)}, \quad \lambda_{h\sigma} = -\frac{M_h^2}{v_h^2+v_\sigma^2}. \tag{2.7}
$$

The rotation matrix $\boldsymbol{R}$ that rotates $\mathbf{M_s}^2$ from flavour to mass eigenstate,

$$
\boldsymbol{R} = \begin{pmatrix}
1 & 0 & 0 & 0 & 0 & 0 \\
0 & 1 & 0 & 0 & 0 & 0 \\
0 & 0 & \frac{-v_\sigma}{\sqrt{v_h^2+v_\sigma^2}} & \frac{v_h}{\sqrt{v_h^2+v_\sigma^2}} & 0 & 0 \\
0 & 0 & \frac{v_h}{\sqrt{v_h^2+v_\sigma^2}} & \frac{v_\sigma}{\sqrt{v_h^2+v_\sigma^2}} & 0 & 0 \\
0 & 0 & 0 & 0 & 1 & 0 \\
0 & 0 & 0 & 0 & 0 & 1
\end{pmatrix}. \tag{2.8}
$$

The matrix $\boldsymbol{R}^T {\mathbf{M_s}}^2 \boldsymbol{R}$ at the minimum is thus

$$\boldsymbol{R}^T {\mathbf{M_s}}^2 \boldsymbol{R} = \begin{pmatrix} 0 & 0 & 0 & 0 & 0 & 0 \\ 0 & 0 & 0 & 0 & 0 & 0 \\ 0 & 0 & M_h^2 & 0 & 0 & 0 \\ 0 & 0 & 0 & 0 & 0 & 0 \\ 0 & 0 & 0 & 0 & 0 & 0 \\ 0 & 0 & 0 & 0 & 0 & 0 \end{pmatrix}, \tag{2.9}$$

clearly demonstrating that the Goldstone bosons, G_1, G_2, and $G_\pm$, and the pseudo Goldstone boson σ are massless at tree-level at the minimum.

2.3.2 One-Loop Corrections

The effective potential, at zero temperature, is the sum of the tree level and one-loop level contributions,

$$V_{\text{eff}} = V_{\text{tree}} + V_{CW} + V_{CT}. \tag{2.10}$$

The Coleman-Weinberg contributions are the effective potential corrections at one-loop level [8, 32, 33],

$$V_{CW} = \frac{1}{64\pi^2} \sum_a (-1)^{2s_a} Q_a N_a (2s_a + 1) M_a^4 \left(\log\left(\frac{M_a^2}{\mu^2}\right) - c_a \right). \tag{2.11}$$

Here s_a is the spin of particle a, Q_a is 2 for charged particles, and 1 for uncharged particles, N_a is 3 for particles with colour, and 1 for particles without colour, and c_a is $\frac{3}{2}$ for fermions and scalars, and $\frac{5}{6}$ for vectors. μ is the renormalisation scale, and M_a is the field-dependent mass of particle a.
The counterterm potential is set up as described in [33], following the description of the on-shell scheme, as carefully described in Refs. [34, 35], with modification to account for the massless physical scalar at tree-level.

$$V_{CT} = V_{\text{tree}}(\lambda \to \delta\lambda) + \delta T_h(\phi_h + h_r) + \delta T_\sigma(\phi_\sigma + h_r') + \delta\mu_h^2(\mathcal{H}^\dagger\mathcal{H}) + \delta\mu_\sigma^2(S^* S) \tag{2.12}$$

Renormalisation conditions are imposed, which at one-loop level are

$$\left.\frac{\partial(V_{CW} + V_{CT})}{\partial\psi_i}\right|_{\phi_h = v_h, \phi_\sigma = v_\sigma} = 0, \tag{2.13}$$

which are the tadpole conditions at one-loop level. From this, δT_h and δT_σ are determined. Then the Hessian of the one-loop corrections is found, and as per definition, the masses at one-loop level in an on-shell-like scheme are equal to the tree-level masses, besides σ, which acquires mass at one-loop as a pseudo-Goldstone boson. The remaining counterterm constants are found following the constraints on the one-loop mass corrections,

$$\left.\mathbf{R}^T \frac{\partial^2(V_{CW} + V_{CT})}{\partial\psi_i\partial\psi_j} \mathbf{R}\right|_{\phi_h = v_h, \phi_\sigma = v_\sigma} = \text{diag}(0, 0, 0, (M_\sigma')^2, 0, 0). \tag{2.14}$$

The one-loop Hessian is rotated by the same rotation matrix $\boldsymbol{R}$ as shown in Equation 2.8,and it is set to equal matrix $\mathbf{M^2_{1-l}}$, that gives the one-loop corrections,

$$\mathbf{M^2_{1-l}} = \begin{pmatrix} 0 & 0 & 0 & 0 & 0 & 0 \\ 0 & 0 & 0 & 0 & 0 & 0 \\ 0 & 0 & 0 & 0 & 0 & 0 \\ 0 & 0 & 0 & (M'_\sigma)^2 & 0 & 0 \\ 0 & 0 & 0 & 0 & 0 & 0 \\ 0 & 0 & 0 & 0 & 0 & 0 \end{pmatrix} . \tag{2.15}$$

Here M'_σ is the mass assigned to σ at VEV by the modified on-shell prescription. The remaining counterterms are determined from the Hessian, and are reproduced in full in the Appendix B.

2.3.3 Finite-Temperature Corrections

The thermal functions for bosons and fermions respectively are

$$\begin{aligned} J_B(y) &= \int_0^\infty dk\ k^2 \log\left(1 - e^{-\sqrt{k^2+y}}\right), \\ J_F(y) &= \int_0^\infty dk\ k^2 \log\left(1 + e^{-\sqrt{k^2+y}}\right), \end{aligned} \tag{2.16}$$

with $y = \frac{M_i^2}{T^2}$. Using the thermal functions, the finite temperature corrections can be written as

$$V_{T,1}(\phi_h, \phi_\sigma, T) = \frac{T^4}{2\pi^2}\left[\sum_b n_b J_B\left(\frac{M_b^2}{T^2}\right) + \sum_f n_f J_F\left(\frac{M_f^2}{T^2}\right)\right], \tag{2.17}$$

where n_b and n_f are the corresponding bosonic and fermionic multiplicities.
The leading infrared divergences can be summed over in a process called 'Daisy resummation', where the divergences are treated to arise from thermal mass corrections [2]. The 'Daisy resummation' method used here is the Arnold-Espinosa method, which can be written as follows, up to field-independent terms [26],

$$V_{\text{Daisy}} = -\frac{T}{12\pi}\sum_{\tilde{B}}\left[(M_{\tilde{B}}^2 + \Pi_{\tilde{B}})^{3/2} - M_{\tilde{B}}^3\right]. \tag{2.18}$$

Here, $\tilde{B}$ describes the bosons receiving thermal corrections. Gauge bosons only receive thermal corrections to their longitudinal masses, while transverse masses remain unchanged. The thermal self-energy correction for boson $\tilde{B}$ are $\Pi_{\tilde{B}}$, as listed in 2.19 [7, 25, 36, 37],

$$
\begin{aligned}
\Pi_\gamma &= \frac{11}{6}g_1^2T^2, \quad \Pi_{W^\pm} = \frac{11}{6}g_2^2T^2, \quad \Pi_{Z^0} = \frac{11}{6}g_2^2T^2, \quad \Pi_{Z'} = \frac{7}{2}g_{B-L}^2T^2, \\
\Pi_h &= \left(\frac{3g_2^2+g_1^2}{16} + \frac{1}{4}y_t^2 + \frac{\lambda_h}{2} + \frac{\lambda_{h\sigma}}{6}\right)T^2, \\
\Pi_\sigma &= \left(g_{B-L}^2 + \frac{\lambda_\sigma}{3} + \frac{\lambda_{h\sigma}}{3}\right)T^2, \\
\Pi_{G_1} &= \left(\frac{3g_2^2+g_1^2}{16} + \frac{1}{4}y_t^2 + \frac{\lambda_h}{2} + \frac{\lambda_{h\sigma}}{6}\right)T^2, \\
\Pi_{G_2} &= \left(g_{B-L}^2 + \frac{\lambda_\sigma}{3} + \frac{\lambda_{h\sigma}}{3}\right)T^2, \\
\Pi_{G_\pm} &= \left(\frac{3g_2^2+g_1^2}{16} + \frac{1}{4}y_t^2 + \frac{\lambda_h}{2} + \frac{\lambda_{h\sigma}}{6}\right)T^2.
\end{aligned}
\tag{2.19}
$$

Thus the full effective potential, V_{eff}, can be constructed as shown in Equation 2.20.

$$
V_{\text{eff}} = V_{\text{tree}} + V_{CW} + V_{CT} + V_{T,1} + V_{\text{Daisy}} \tag{2.20}
$$

The full effective potential is plotted at background condition, for varying values of M'_σ, both at $T = 0$ GeV, and at $T = 500$ GeV, as shown in Figure 1, and Figure 2. The standard plotting parameters used for all plots in this section, unless specified otherwise, are given in Table 2.

Plotting Parameter	Constant Used
v_h	246 GeV
M_h	125.1 GeV
ϕ_h	v_h
v_σ	1000 GeV
M'_σ	450 GeV
g_1	negligible for illustrative purpose
g_2	negligible for illustrative purpose
g_{B-L}	0.3
μ	v_σ
y_t	1

Table 2: The standard plotting parameters used for graphs.

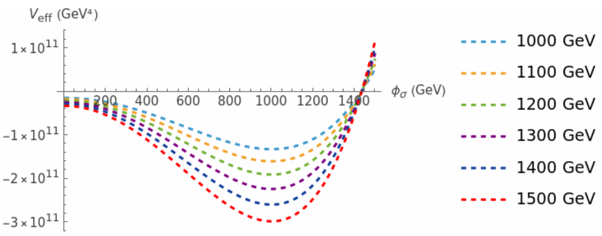

Figure 1: The effective potential for varying M'_σ and $T = 0$ GeV.

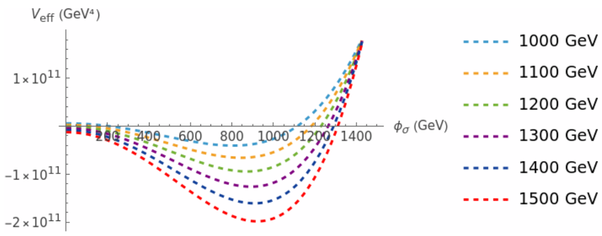

Figure 2: The effective potential for varying M'_σ and $T = 1500$ GeV.

The minima in Figure 1, do not move for different values of M'_σ, as fixed by the modified on-shell scheme, however, the minima shift as temperature increases, as shown in Figure 2, as the thermal corrections modify the shape of the effective potential, as expected from Equation 2.18.

The full effective potential is plotted for different temperatures, showing features vital to the FOPT discussed later in Section 3. Figure 4 illustrates the high-temperature regime, where the origin is the relevant minimum. As the universe cools, a second minimum away from the origin develops; near the critical temperature the two minima become degenerate, and below it the broken minimum becomes energetically favoured, as illustrated in Figure 3.

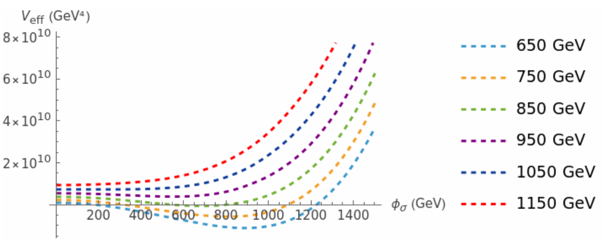

Figure 3: The effective potential for varying T, demonstrating the formation of the false and true vacuum.

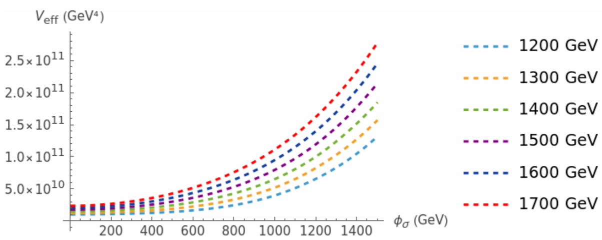

Figure 4: The effective potential for varying T, demonstrating the global minima at the origin for high temperature.

The effective potential is plotted for differing values of g_{B-L}, shown in Figure 5 demonstrating the modified on-shell schemes characteristic of not shifting the minima from v_σ, a feature further seen in Figure 6, where different values of v_σ are plotted.

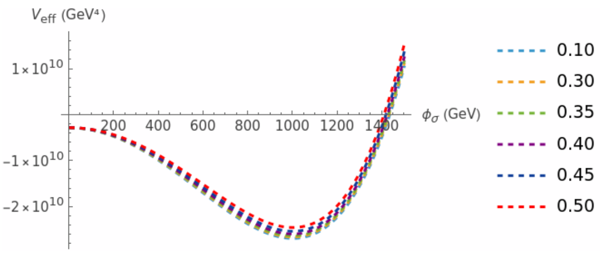

Figure 5: The effective potential for varying g_{B-L} and $T = 0$ GeV.

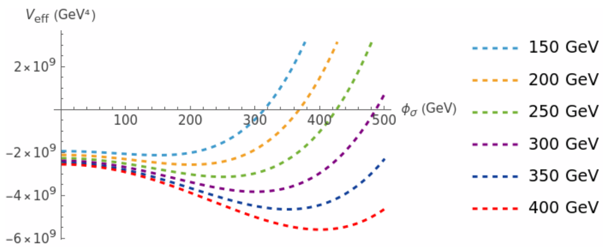

Figure 6: The effective potential for varying v_σ and $T = 0$ GeV.

3 FOPT and gravitational waves

At non-zero temperature, the shape of the effective potential changes, as illustrated in Section 2.3.3. At sufficiently high temperature the origin is typically the preferred minimum, but as the universe cools, a second minimum can develop away from the origin. Near the critical temperature T_c the two minima are degenerate, and below T_c the broken minimum becomes energetically favoured while the origin may remain as a metastable false vacuum. Below T_c, quantum tunnelling and thermal fluctuations can nucleate bubbles of the true vacuum.

Another relevant temperature is the percolation temperature, which is defined as the temperature at which the true-vacuum bubbles fill enough of the universe to form a connected network [8]. A commonly used criterion is the true vacuum fraction $I(T_p) \simeq 0.34$ [29, 38]. Lastly, the nucleation temperature is the temperature at which the nucleation of true vacuum bubbles begins.

The bubble nucleation rate is commonly approximated as [7, 8, 39],

$$\Gamma(T) \simeq T^4 \left(\frac{S_3}{2\pi T}\right)^{3/2} e^{-S_3/T}.$$

Therefore, the nucleation temperature, T_n, can be estimated by roughly requiring one critical bubble per Hubble volume, a sphere with radius $r = \frac{1}{H_T}$, per Hubble time, $\frac{1}{H_T}$, [8, 25],

$$\left.\frac{\Gamma}{H_T^4}\right|_{T=T_n} = 1,$$

where H_T is the Hubble parameter.

S_3 is the action of the bubble, such that

$$S_3 = 4\pi \int r^2 dr \left(\frac{1}{2}\left(\frac{d\phi}{dr}\right)^2 + V_{\text{eff}}(\phi, T) - V_{\text{eff}}(\phi_f, T)\right). \tag{3.1}$$

The action is minimised by the bounce solution $\phi(r)$, which obeys [2, 40]

$$\frac{dV_{\text{eff}}}{d\phi} = \frac{d^2\phi}{dr^2} + \frac{2}{r}\frac{d\phi}{dr}, \quad \left.\frac{d\phi}{dr}\right|_{r=0} = 0, \quad \phi(r \to \infty) = \phi_f. \tag{3.2}$$

ϕ_f denotes the field value of the false vacuum. GWs created by FOPT can be described using five thermodynamic parameters; transition temperature, transition strength, reheating temperature, bubble wall velocity, and characteristic length scale [2, 11, 41].
The transition temperature, T_*, is the temperature at which the phase transition is evaluated for the gravitational-wave calculation. In the rest of this thesis, subscript '$*$' refers to evaluation at $T = T_*$. For rapid transitions one often uses the nucleation temperature T_n, whereas for strongly supercooled transitions the percolation temperature T_p is usually more appropriate, because gravitational waves are mainly generated when bubbles have grown and started to collide [2]. This choice is discussed further in Section 3.1.

The transition strength α measures the released vacuum energy density relative to the radiation energy density of the plasma. Larger values generally lead to stronger GW signals, although the final amplitude also depends on the wall velocity, efficiency factors and the characteristic length scale. A commonly used estimate is [2, 28]

$$\alpha_* = \frac{\Delta V_{\text{eff}}(T_*) - \frac{T_*}{4}\Delta(\partial_T V_{\text{eff}})_{T_*}}{\rho_{\text{rad}}(T_*)}, \quad \rho_{\text{rad}}(T_*) = \frac{\pi^2}{30} g_* T_*^4, \tag{3.3}$$

Here $\Delta X \equiv X(\phi_t, T_*) - X(\phi_f, T*)$ denotes the difference between the false- and true vacuum values, where ϕ_t is the true vacuum field value, and the derivative is evaluated at T_*. Here g_* is the effective number of degrees of freedom (dof) at the end of the phase transition, this includes the dof of the SM, the σ scalar, and the massive Z' gauge boson [8, 10]. The effective degrees of freedom, g_* can be approximated to $g_* \approx 100$ for $T > 100$ GeV [42].
The reheating temperature T_{RH} characterizes the temperature of the radiation bath after the latent vacuum energy has been released. T_{RH} is evaluated as follows [43], which can be approximated for strongly supercooled transitions,

$$T_{RH} = \left(\frac{\Gamma_\sigma}{H_*}\right)^{1/2} T_*(1+\alpha_*)^{\frac{1}{4}} \overset{\alpha \gg 1}{\approx} T_*(1+\alpha_*)^{1/4}, \tag{3.4}$$

where Γ_σ describes the decay rate of the ϕ_σ field [44], but this decay width is not computed explicitly in the benchmark analysis in Section 4. The other thermodynamic parameters are not affected by T_{RH}, and thus are to be taken at transition temperature [2, 8].
The bubble wall velocity, v_w, is the speed at which the front of the FOPT progresses [45]. This parameter is an important input for the gravitational-wave spectrum, as discussed further in Section 3.3.
The characteristic length scale R_* describes the mean bubble separation [10]. Some sources, such as Ref. [8] use the inverse time duration, $\frac{\beta}{H_{T_p}}$, where $\frac{\beta}{H_{T_n}} = T_n \frac{d}{dT}\frac{S_3}{T}\Big|_{T=T_n}$ [9], which can be defined in terms of R_*,

$$\frac{\beta}{H_*} = (8\pi)^{\frac{1}{3}} \cdot \frac{\max(v_w, c_s)}{H_* R_*}. \tag{3.5}$$

c_s is the speed of sound in the plasma.
As the thermodynamic parameters are very different based on which model is considered, they will be discussed more in depth in Section 3.1.

3.1 Supercooled FOPT

Supercooling describes a process where the false vacuum remains stable much beyond the critical temperature, thus, supercooled FOPT occur for the transition temperature, $T_* \ll T_c$,[5, 7]. The reference temperature used is the percolation temperature T_p, as the FOPT is very slow [29],[38], see also Figures 10, 12 in the appendix D. The reheating temperature, T_{RH}, for strongly supercooled FOPT is $T_{RH} \simeq T_p(1+\alpha)^{\frac{1}{4}}$,where after percolation the universe reheats to a radiation dominated space [41]. For very strong transitions it is common, but still model-dependent, to approximate the bubble walls as ultra-relativistic, $v_w \simeq 1$ [9, 46].

3.2 Gravitational-wave production

The energy released during a FOPT is distributed among scalar-field gradients, bulk motion of the plasma, and reheating. The three distinct processes resulting in gravitational waves are:
(i) collisions of the bubble walls, (ii) sound waves in the plasma, and (iii) magnetohydrodynamic turbulence [8, 9, 47, 48]. The gravitational waves produced through these processes contribute to the stochastic gravitational wave background (SGWB) [8, 9],

$$h^2\Omega_{GW}(f) = \frac{h^2}{\rho_c}\frac{d\rho_{GW}}{d\log f}. \tag{3.6}$$

Here $h^2\Omega_{GW}$ describes the energy density due to the GW contributions, h is such that $H_0 = 100\ h$ km/s/Mpc [49], while f is the frequency, ρ_{GW} is the energy density of the gravitational wave, and $\rho_c = \frac{3H^2}{8\pi G}$, which is the critical energy density today. The contributions of each source can be linearly combined, thus $h^2\Omega_{GW} \simeq h^2\Omega_{\rm col} + h^2\Omega_{\rm sw} + h^2\Omega_{\rm turb}$.
The gravitational wave contributions can be described via a general equation,

$$h^2\Omega = h^2 \cdot F_{GW,0} \cdot S_{\rm scaling}(\alpha, v_w, \beta, H) \cdot S_{\rm shape}(f). \tag{3.7}$$

The $F_{GW,0}$ term represents the redshift corrections. Since these waves originate in the very early universe, the spectrum needs to be adjusted to account for redshifting due to the expansion of the universe,

$$h^2F_{GW,0} \simeq 1.64 \cdot 10^{-5}\left(\frac{100}{g_*}\right)^{\frac{1}{3}}. \tag{3.8}$$

The $S_{\text{scaling}}(\alpha, v_w, \beta, H)$ term describes the scaling of the gravitational wave based on the thermodynamic constants and differs for each source of GWs. Notably the term depends on H_* and $H_{*,0}$, which are the Hubble constant at the transition temperature and the Hubble constant at the transition temperature redshifted to today respectively.

$$
\begin{aligned}
H_*^2 &= \frac{\rho_{\text{tot}}(T_*)}{3M_{Pl}^2}, \qquad \rho_{\text{tot}}(T_*) \simeq \rho_{\text{rad}}(T_*) + \rho_{\text{vac}}(T_*). \\
H_{*,0} &= \frac{a_*}{a_0} H_* \simeq 1.65 \cdot 10^{-5}\text{Hz} \left(\frac{g_*}{100}\right)^{\frac{1}{6}} \left(\frac{T_{RH}}{\text{GeV}}\right) \left(\frac{\Gamma_\sigma}{H_*}\right)^{\frac{2}{3}}.
\end{aligned} \tag{3.9}
$$

M_{Pl} is the reduced Planck mass, $M_{Pl} \approx 2.4 \cdot 10^{18}$ GeV, and a_* and a_0 are the scale factors at the transition and today, respectively [2]. In the radiation-dominated limit H_* reduces to $H_* \simeq 1.66\sqrt{g_*}\,T_*^2/M_{Pl}$.

The shape term $S_{\text{shape}}(f)$ describes the shape of the gravitational power spectrum, and thus varies with f. This term takes different forms for the different gravitational wave sources, as further elaborated upon below.

3.2.1 Bubble Collisions

The contributions of Ω_{col} to Ω_{GW} are thought to be dominant for a significantly supercooled FOPT [9, 47]. The gravitational waves due to these collisions can be evaluated using an approximation called the envelope approximation [47, 50–52], rather than the more imprecise dimensional analysis [9]. The envelope approximation considers the energy density within the true vacuum bubbles to be very small compared to the energy stored in the bubble walls, thus the gravitational wave production does not depend on the scalar field, but instead on the shape of the bubbles colliding [47, 51, 53]. This approach has been criticised in more recent publications [10, 54]. Numerical results obtained for this model by Ref. [51] derive

$$
\begin{aligned}
h^2\Omega_{\text{col}} &= 1.67 \cdot 10^{-5} \left(\frac{H_T}{\beta}\right)^2 \left(\frac{\kappa\alpha}{1+\alpha}\right)^2 \left(\frac{100}{g_*}\right)^{\frac{1}{3}} \frac{0.11 v_w^3}{0.42 + v_w^2} S_v(f), \\
S_v(f) &= \frac{3.8\left(\frac{f}{f_0}\right)^{2.8}}{1 + 2.8\left(\frac{f}{f_0}\right)^{3.8}}.
\end{aligned} \tag{3.10}
$$

The constants are defined as follows: κ is the fraction of energy released in the FOPT converted to kinetic energy, f_0 is the peak frequency of the spectrum today, which can be determined using

$$
f_0 = 16.5 \cdot 10^{-3}\text{mHz} \left(\frac{f_T}{\beta}\right) \left(\frac{\beta}{H_T}\right) \left(\frac{T}{100\text{GeV}}\right) \left(\frac{g_*}{100}\right),
$$

with f_T being the peak frequency at temperature T.
The proposed alternative model, as described in Ref. [10], takes the form of a broken power law,

$$\Omega_{\rm col}(f, \Omega_p, f_p) = \Omega_p \frac{(n_1 - n_2)^{\frac{n_1-n_2}{a_1}}}{\left(-n_2\left(\frac{f}{f_p}\right)^{\frac{-n_1 a_1}{n_1-n_2}} + n_1\left(\frac{f}{f_p}\right)^{\frac{-n_2 a_1}{n_1-n_2}}\right)^{\frac{n_1-n_2}{a_1}}}, \tag{3.11}$$

where Ω_p and f_p correspond to the peak amplitude and peak frequency respectively, and following the example set in Ref [8], they will be referred to as geometric parameters. The thermodynamic parameters relate to the geometric parameters [8, 10],

$$\begin{aligned} h^2\Omega_p &= h^2 F_{GW,0} A \left(\frac{\alpha}{1+\alpha}\right)^2 \left(\frac{H_*}{\beta}\right)^2, \\ f_p &\simeq 0.11 H_{*,0} \frac{\beta}{H_*}. \end{aligned} \tag{3.12}$$

For a strongly supercooled model, the following has been numerically determined by Ref. [55]: $A \simeq 0.05, n_1 = -n_2 \simeq 2.4, a_1 \simeq 1.2$, and the prefactor of 0.11 for the definition of f_p.

3.2.2 Sound waves

The sound wave contributions, $\Omega_{\rm sw}$, can be estimated using the Sound Shell model [56, 57]. The Sound Shell model uses the fact that expanding bubbles induce sound waves in the plasma, which persist after the bubbles have collided. These sound waves superpose, and the velocity in the plasma is thus approximated as a Gaussian random field, made up of the contribution of a large number of sound shells [2, 56, 57]. The $S_{\rm shape}(f)$ factor of the sound wave contributions take the form of a double broken power law, as shown in Equation 3.13 [8, 10, 57–59]. The $F_{GW,0}$ and $S_{\rm scaling}$ terms are included within $\Omega_{\rm int}$, where the full analytical contributions are given in Appendix C.1 It is worth noting that in sufficiently strong supercooled FOPT, the bubbles do not reach a constant velocity, and continue to accelerate until collision, rendering the Sound Shell model invalid [2, 57], and in that case Ref. [57] recommends the use of the envelope approximation [51] for an order-of-magnitude estimate for the gravitational wave spectrum.

$$\begin{aligned} h^2\Omega_{\rm sw}(f, f_1, \Omega_2, f_2) &= \Omega_{\rm int} \times S(f), \\ S(f) &= N\left(\frac{f}{f_1}\right)^{n_1}\left(1+\left(\frac{f}{f_1}\right)^{a_1}\right)^{\frac{-n_1+n_2}{a_1}}\left(1+\left(\frac{f}{f_2}\right)^{a_2}\right)^{\frac{-n_2+n_3}{a_2}}. \end{aligned} \tag{3.13}$$

From Ref. [58], the following parameters are determined: $n_1 = 3, n_2 = 1, n_3 = -3, a_1 = 2$, and $a_2 = 4$.

3.2.3 Magnetohydrodynamic Turbulence

The last contributions to Ω_{GW} is due to turbulence, Ω_{turb}. Turbulence arises from non-linearities in the sound-wave fluid motion, and is assumed to persist after the coherent sound waves have dissipated [60]. The contributions of $\Omega_{\text{turb}} = \Omega_M + \Omega_K$, where the energy density is equally distributed among the energy density of the magnetic contributions, Ω_M, and the kinetic contributions, Ω_K [10, 60, 61]. The shape factor $S_{\text{shape}}(f)$ of Ω_{turb} has the form of a double broken power law, as shown in Equation 3.14 , where the $F_{GW,0}$ and S_{scaling} terms are within Ω_2 [10, 60]. The full analytical expression for Ω_{turb} is given in Appendix C.2.

$$
\begin{aligned}
h^2\Omega_{\text{turb}} &= \Omega_2 \times S_2(f), \\
S_2(f) &= 2^{\frac{11}{3a_2}} \left(\frac{f_1}{f_2}\right) \left(\frac{f}{f_1}\right)^3 \left(1 + \left(\frac{f}{f_1}\right)^{a_1}\right)^{\frac{-2}{a_1}} \left(1 + \left(\frac{f}{f_2}\right)^{a_2}\right)^{\frac{-11}{3a_2}}.
\end{aligned} \tag{3.14}
$$

The parameters are found to be as follows: $a_1 = 4$ and $a_2 \simeq 2.15$ [10].

3.3 Gravitational wave analysis

The numerical calculations for the resultant GWs arising due to the FOPT dynamics described, will be done using the `TransitionSolver` package [27–29]. The bubble wall velocity, v_w, can analytically be derived, as shown in Ref. [51], however, as discussed in said paper using Ref. [62], this is simply a lower bound, and thus v_w will be found in terms of bounds [29]. Using the `TransitionSolver` package, the gravitational wave spectrum will be compared to the ranges of LISA [15, 16]and to NANOGrav[12], PPTA[13], and EPTA [14] data. Furthermore, the models implemented will be compared to the results found in Ref. [8], for a class of generic classically conformal $U'(1)$ extension.

The full two-field analytical model of Section 2 is not implemented numerically in this thesis. Instead, two related benchmark implementations are studied: first, a one-field conformal $B-L$ limit available in `TransitionSolver`, newly released for Ref. [21], and second, a $U(1)$+complex-singlet proxy model with an on-shell-like scalar-sector prescription. These benchmarks are used to explore qualitative features of supercooling and renormalization-scheme choices rather than to provide a complete phenomenological scan of the full model.

The model used in Ref. [21] describes a classically conformal $B - L$ model, simplified to the limit $v_\sigma \gg v_h$, thus leading to the discussed FOPT to be almost entirely decoupled from the Higgs scale. This approximation is motivated by the hierarchy between the electroweak and $B - L$-breaking scales. If the conventional normalization $M_{Z'} = 2g_{B-L}v_\sigma$ is used, a representative collider lower bound $M_{Z'} \gtrsim 5$ TeV implies $g_{B-L}v_\sigma \gtrsim 2.5$ TeV, or equivalently $g_{B-L}^2 v_\sigma^2 \gtrsim 6.25$ TeV^2 [8, 63–65]. For $g_{B-L} = 0.05$ this gives $v_\sigma \gtrsim 50$ TeV, already well above the electroweak scale. The much larger benchmark values used below

therefore safely lie in the decoupling regime. It does differ from the model described in Section 2 considerably, as it uses the $\overline{MS}$ scheme, rather than the on-shell scheme, and the simplification discussed eliminates the ϕ_h field direction. The model thus has the following properties:
$V_{\text{tree}} = \lambda_\sigma[S^*S]^2$, and only includes Z' boson and massive RHN contributions at one-loop level and regarding the thermal contributions. Furthermore, M_σ is assumed to be small and thus scalar contributions are not included [21].

The schematic one-field ingredients relevant for the comparison are summarised below:

$$\begin{aligned} V_{\text{tree}} &= \lambda_\sigma (S^*S)^2, \\ M_{Z'}^2(\phi_\sigma) &= 4g_{B-L}^2\phi_\sigma^2, \qquad M_{\nu_{R,i}}^2(\phi_\sigma) = \frac{\lambda_{R_i}^2}{2}\phi_\sigma^2 \\ V_{CW} &\supset \frac{3M_{Z'}^4}{64\pi^2}\left[\log\left(\frac{M_{Z'}^2}{\mu^2}\right) - \frac{5}{6}\right] - \sum_i \frac{2M_{\nu_{R,i}}^4}{64\pi^2}\left[\log\left(\frac{M_{\nu_{R,i}}^2}{\mu^2}\right) - \frac{3}{2}\right]. \end{aligned} \tag{3.15}$$

The precise finite-temperature and daisy-resummed contributions are evaluated inside the `TransitionSolver` implementation used for Ref. [21].

The second model implemented in `TransitionSolver` is a $U(1)$+complex-singlet extension of the Standard Model. It should be viewed as an on-shell-like proxy model rather than as the full gauged $B-L$ model of Section 2, because the SM fermions are not charged under the additional $U(1)$. It further differs from the analytical model as the Gildener-Weinberg "scalon" is set to be the Standard Model Higgs boson, thus the σ boson obtains mass at tree level, which is fixed at one-loop level using the on-shell scheme. This model is not taken at the limit $v_\sigma \gg v_h$. It retains both field directions, but simplifies the Z' sector, giving $\Pi_{Z'} = \frac{4}{3}g_{B-L}^2 T^2$. Since the Z' does not couple to fermions in this proxy implementation, RHN contributions are absent.

4 Numerical Results

The results were obtained as described in Section 3.3, using the `TransitionSolver` python module [27–29].
The $B-L$ model can be effectively approximated, as described in Section 3.3. The results obtained using the code for Ref. [21], were computed using the following input parameters: $v_\sigma = 100000$ TeV, $g_{B-L} = 0.05$, $\lambda_2 = \lambda_3 = 1.2$, and $\lambda_1 = 0.3$. The code includes an extra complex singlet, which was removed by setting $\lambda'_S = 0$. As described in Section 3.3, this results in a light, stable RHN as a dark matter candidate, and two heavier RHNs that the σ decays via, and that decay into the dark matter candidate, as described in Ref. [21].
The gravitational wave amplitude diagram is shown in Figure 7. Furthermore, `TransitionSolver` calculates the development of key parameters against temperature,

which are shown in Figures 10 and 11, and an extensive list of key parameters is reproduced in Table 3, in the Appendix D. The transition strength is then calculated from Equation 3.3, at $T_* = T_p$, where α_* is found as $\alpha_* \gtrsim 10^{13}$.

The second set of results is obtained for the $U(1)$ and complex singlet extension model described in Section 3.3, with input parameters as follows:
$v_\sigma = 5$ TeV, $M_\sigma = 1$ TeV, $g_{B-L} = 0.3$, and the remaining parameters as given by the Standard Model, with $\mu = v_\sigma$. As σ in this model is not a pseudo Goldstone boson, its tree-level mass at VEV is M_σ. Furthermore, as the Higgs boson is the pseudo Goldstone in this model, the tree-level mass M_h at VEV is zero, thus the mass fixed to the Standard Model Higgs mass is the one-loop level mass, M_h'. The diagram of gravitational wave amplitude is shown in Figure 8.

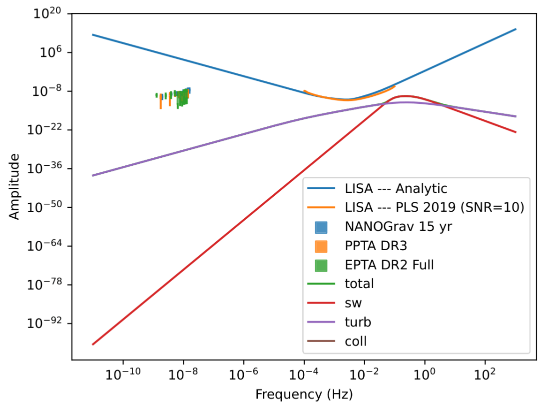

Figure 7: Gravitational-wave power spectrum for the one-field $v_\sigma \gg v_h$ conformal $B-L$ benchmark with RHN contributions, plotted against PTA [12–14] data and LISA sensitivity [15, 16].

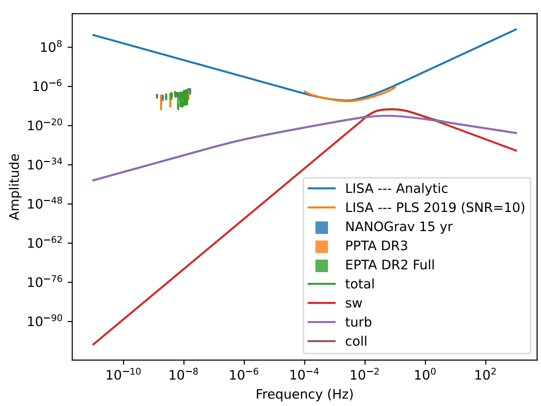

Figure 8: Gravitational-wave power spectrum for the $U(1)$+complex-singlet proxy model with an on-shell-like prescription, plotted against PTA [12–14] data and LISA sensitivity [15, 16] .

The labels refer to the following: The analytically determined LISA sensitivity curve, the power-law sensitivity curve for LISA [16], NANOGrav data [12], PPTA data [13], EPTA data [14], the total gravitational wave plot for the model, the soundwave contributions to the gravitational wave spectrum, the turbulence contributions to the gravitational wave spectrum, and the bubble collision contributions to the gravitational wave spectrum.
The total contribution plots are not visible due to the strongly logarithmic nature of the plots, leading them to be obscured by the turbulence and sound wave contributions.

The development of key parameters with temperature is given by Figures 12 and 13, and the final set of parametric results is given by Table 4, found in Appendix D. The results obtained from `TransitionSolver` for the 'Higgs scalon' model can be used to obtain the transition strength α_*. This yields $\alpha_* \gtrsim 261$, at $T_* = T_p$, the implications will be discussed in the next section, Section 4.1.

4.1 Discussion

For both benchmark models, the predicted gravitational-wave spectra are below the nominal LISA detectability threshold and do not overlap with the current PTA-favoured region. For the simplified $B-L$ benchmark, the peak sound-wave amplitude is $\Omega_{\text{sw,peak}} = 1.7735 \cdot 10^{-10}$. The amplitude is relatively large, but the peak frequency lies outside the most sensitive part of the LISA band, as shown in Figure 7. The corresponding signal-to-noise ratios are $SNR_{\text{LISA,analytic}} = 0.22911$ and $SNR_{\text{LISA,PLS}} = 0.46580$, below the usual detectability criterion $SNR > 10$ [8].
The peak amplitude for the 'Higgs scalon' model is $\Omega_{\text{sw,peak}} = 7.1306 \cdot 10^{-15}$. This is below LISA range, this could be due to the lower Debye mass of Z' due to the lack of fermion coupling, or the light σ. The SNR is found as $SNR_{\text{LISA,analytic}} = 0.00061716, SNR_{\text{LISA,PLS}} = 0.0026537$, and thus as expected, is nowhere close to detectable.

The relationship between $M_{Z'}$, peak frequency, and peak gravitational-wave amplitude was plotted, using a set of parameters generated from $g_{B-L} = [0.2, 0.5]$, and $v_\sigma = [5 \text{ TeV}, 10 \text{ TeV}]$. This is shown in Figure 9 below.

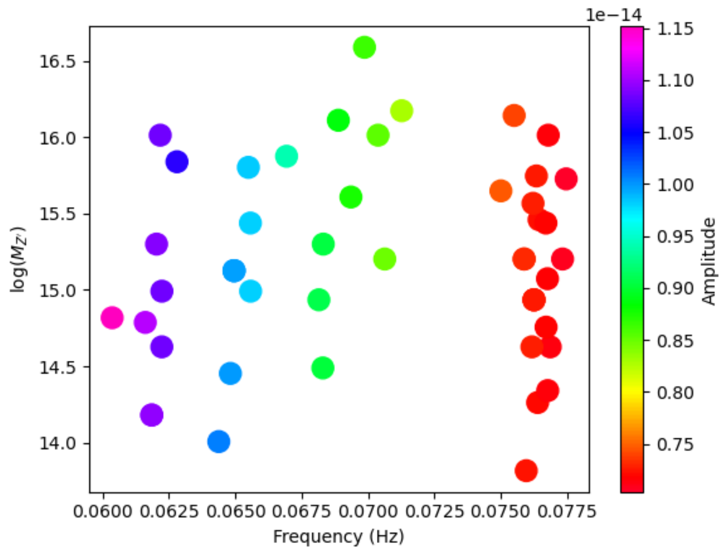

Figure 9: Peak frequency and amplitude for the scanned proxy model benchmark points, with the colour scale indicating $\log(M_{Z'})$.

The parameter $M_{Z'}$ furthermore does not reproduce the results shown in Ref. [8], as $M_{Z'}$ seems to not affect the gravitational wave spectrum strongly. This might be due to the lower $\Pi_{Z'}$, or due to the low number and range of data points studied.

In both benchmarks the gravitational-wave spectrum is evaluated at the percolation temperature. For the simplified $B-L$ benchmark one finds $T_p = 11325$ GeV, $T_c = 29216$ GeV and $T_{RH} = 15288$ GeV. This indicates significant supercooling, with $T_p < T_n < T_c$, and is qualitatively consistent with the high-scale supercooled examples discussed in Ref. [8]. The large value of α_* obtained in this benchmark reflects the dominance of released vacuum energy over the radiation bath within the adopted thermodynamic prescription. The numerically obtained value $v_{w,p} = 0.95836$ also supports the use of an ultra-relativistic wall-velocity approximation for this benchmark.

For the $U(1)$+complex-singlet proxy model, the transition occurs at a much lower scale, with $T_p = 113.85$ GeV and $T_c = 126.61$ GeV. The hierarchy $T_p/T_c \simeq 0.90$ indicates only modest supercooling in temperature, even though the thermodynamic strength parameter obtained from the adopted prescription is large, $\alpha_* \gtrsim 261$. The result $T_{RH} = 127.87$ GeV $> T_c$ suggests that reheating can bring the plasma back above the critical temperature in this benchmark. This behaviour should be interpreted cautiously and studied further in a complete implementation, rather than taken as a generic prediction of the model. Larger values of α_* often enhance the gravitational-wave amplitude, but the final signal also depends sensitively on β/H_*, R_*, the efficiency factor κ, the wall velocity and the source model. Therefore the observed amplitudes should be interpreted at the benchmark level rather than as a universal consequence of α_* alone.

5 Conclusion and Outlook

This thesis has described the dynamics of first-order phase transitions in classically conformal $B-L$-like models, with emphasis on the thermodynamic parameters relevant for gravitational-wave production. A $B-L$-like model under a modified on-shell scheme was analytically described, and used to demonstrate the characteristics of the modified on-shell scheme. The finite-temperature effective potential was used to discuss supercooling, bubble nucleation, percolation and reheating, while the resulting stochastic gravitational-wave spectra were estimated using standard phenomenological descriptions of bubble collisions, sound waves and turbulence.

Numerical results were obtained with TransitionSolver for two benchmark implementations: a simplified one-field conformal $B-L$ model and an on-shell-like $U(1)$+complex-singlet proxy model. For the benchmark points studied here, the predicted gravitational-wave spectra have signal-to-noise ratios below the nominal LISA detectability threshold and do not overlap with the current PTA-favoured region. This conclusion applies only to the limited benchmark points considered, not to the full parameter space of the model class.

The impact of an on-shell-like prescription on the phase-transition dynamics remains an open question. The present analysis shows that such a prescription can be explored within numerical phase-transition tools, but a complete implementation of the full analytical model and a systematic parameter scan are required before drawing robust phenomenological conclusions.

Within the adopted thermodynamic prescription, the large values of α indicate strongly supercooled transitions in the studied benchmarks. The next step is therefore to implement the full analytical model consistently, verify the counterterm and finite-temperature conventions, and perform a large-scale parameter scan to determine whether detectable signals can arise in viable regions of parameter space.

Acknowledgements

Firstly, I want to express my thanks to my supervisor, Roman Pasechnik, for his quick responses and constant help. I also want to thank Leo Carlsson, Embla Nótt Péturs, Sal Wetzel, and Lynn Sun for their tremendously helpful feedback on the popular abstract. Lastly, I want to thank Dahamvin Bentota Arachchige and Calla Geimer for fruitful discussions regarding the structure and content of this thesis.

A Anomalies

In evaluating anomalies, all fermions are counted as left-handed Weyl fermions, equivalently, right-handed fermions are represented by their left-handed charge-conjugate fields, which accounts for the relative signs below:

$U'(1) \times [SU(3)_c]^2 : 2x_q - x_u - x_d = 2 \cdot \frac{1}{3} - \frac{1}{3} - \frac{1}{3} = 0$

$U'(1) \times [SU(2)_L]^2 : 3x_q + x_\ell = 3 \cdot \frac{1}{3} + (-1) = 0$

$U'(1) \times [U(1)_Y]^2 : x_q - 8x_u - 2x_d + 3x_\ell - 6x_e = \frac{1}{3} - 8 \cdot \frac{1}{3} - 2\frac{1}{3} + 3 \cdot (-1) - 6 \cdot (-1) = 0$

$[U'(1)]^2 \times U(1)_Y : x_q^2 - 2x_u^2 + x_d^2 - x_\ell^2 + x_e^2 = \frac{1}{3}^2 - 2 \cdot \frac{1}{3}^2 + \frac{1}{3}^2 - (-1)^2 + (-1)^2 = 0$

$[U'(1)]^3 : 6x_q^3 - 3x_u^3 - 3x_d^3 + 2x_\ell^3 - x_\nu^3 - x_e^3 = 6 \cdot \frac{1}{3}^3 - 3 \cdot \frac{1}{3}^3 - 3 \cdot \frac{1}{3}^3 + 2 \cdot (-1)^3 - (-1)^3 - (-1)^3 = 0$

$U'(1) \times [grav.]^2 : 6x_q - 3x_u - 3x_d + 2x_\ell - x_\nu - x_e = 6 \cdot \frac{1}{3} - 3 \cdot \frac{1}{3} - 3 \cdot \frac{1}{3} + 2 \cdot (-1) - (-1) - (-1) = 0$

x_a is the $B - L$ charge of particle a.

B Counterterms

The counterterms are obtained by solving the one-loop tadpole and modified on-shell-like mass-renormalization conditions stated in Section 2.3.2. They are evaluated at $(\phi_h, \phi_\sigma) = (v_h, v_\sigma)$, as discussed in Section 2.3.2, and written in terms of the physical input parameters and the renormalization scale.

$$\delta T_h = 0, \quad \delta T_\sigma = 0, \quad \delta\mu_h^2 = \frac{8\left(\frac{3}{v_h^2} - \frac{4}{v_h^2+v_\sigma^2}\right)M_h^4 - 128\pi^2 M_\sigma'^2 + 3v_h^2\left(g_1^4 + 2g_2^2 g_1^2 + 5g_2^4 - 16y_t^4\right)}{256\pi^2},$$

$$\delta\mu_\sigma^2 = \frac{\left(3v_h^2 - v_\sigma^2\right)M_h^4 + v_\sigma^2\left(16\left(v_h^2+v_\sigma^2\right)\left(6g_{B-L}^4 v_\sigma^2 - \pi^2 M_\sigma'^2\right) - 9\log(2) v_h^4 y_t^4\right)}{32\pi^2 v_\sigma^2\left(v_h^2+v_\sigma^2\right)},$$

$$\delta\lambda_\sigma = \frac{8\log\left(\frac{2M_h^2}{\mu^2}\right)\left(3v_h^2 - v_\sigma^2\right)M_h^4 + 48\log\left(\frac{M_h^2}{\mu^2}\right)\left(2v_\sigma^2 - 3v_h^2\right)M_h^4 + 8\left((\log(2)-3)v_\sigma^2 - (\log(8)-3)v_h^2\right)M_h^4}{512\pi^2 v_\sigma^2\left(v_h^2+v_\sigma^2\right)^2}$$
$$+\frac{v_\sigma^2\left(-1024v_\sigma^4 g_{B-L}^4 - 1792v_h^2 v_\sigma^2 g_{B-L}^4 + 3g_1^4 v_h^4 + 15g_2^4 v_h^4 + 6g_1^2 g_2^2 v_h^4 + 144\log(2) v_h^4 y_t^4 + 48v_h^4 y_t^4 + 256\pi^2 M_\sigma'^2\left(v_h^2+v_\sigma^2\right)\right)}{512\pi^2 v_\sigma^2\left(v_h^2+v_\sigma^2\right)^2}$$
$$+\frac{3v_\sigma^2\left(-256\log\left(\frac{4g_{B-L}^2 v_\sigma^2}{\mu^2}\right)v_\sigma^2\left(5v_h^2+2v_\sigma^2\right)g_{B-L}^4 + 12\log\left(\frac{g_2^2 v_h^2}{4\mu^2}\right)g_2^4 v_h^4 + 3\log\left(\frac{\left(g_1^2+g_2^2\right)v_h^2}{4\mu^2}\right)\left(g_1^2+g_2^2\right)^2 v_h^4 - 48\log\left(\frac{v_h^2 y_t^2}{\mu^2}\right)v_h^4 y_t^4\right)}{512\pi^2 v_\sigma^2\left(v_h^2+v_\sigma^2\right)^2},$$

$$
\begin{aligned}
\delta\lambda_h = {} & \frac{-20g_2^4v_h^8-40g_2^4v_\sigma^2v_h^6-5g_2^4v_\sigma^4v_h^4+1024g_{B-L}^4v_\sigma^4v_h^4+48v_\sigma^4y_t^4v_h^4+48\log\left(\frac{v_h^2y_t^2}{\mu^2}\right)\left(2v_h^4+4v_\sigma^2v_h^2-v_\sigma^4\right)y_t^4v_h^4+256\pi^2M_\sigma'^2\left(v_h^2+v_\sigma^2\right)v_h^4}{512\pi^2v_h^4\left(v_h^2+v_\sigma^2\right)^2} \\
& +\frac{g_1^4\left(4(\log(8)-1)v_h^4+4(\log(512)-2)v_\sigma^2v_h^2-(\log(64)+1)v_\sigma^4\right)v_h^4+2g_1^2g_2^2\left(2(\log(512)-2)v_h^4+4(\log(512)-2)v_\sigma^2v_h^2-(\log(64)+1)v_\sigma^4\right)v_h^4}{512\pi^2v_h^4\left(v_h^2+v_\sigma^2\right)^2} \\
& +\frac{3\left(4\log\left(\frac{g_2^2v_h^2}{4\mu^2}\right)v_\sigma^4g_2^4-8\log\left(\frac{g_2^2v_h^2}{\mu^2}\right)v_h^2\left(v_h^2+2v_\sigma^2\right)g_2^4-4\log\left(\frac{2\left(g_1^2+g_2^2\right)v_h^2}{\mu^2}\right)v_h^2\left(g_1^2g_2^2v_h^2+\left(g_1^2+g_2^2\right)^2v_\sigma^2\right)\right)v_h^4}{512\pi^2v_h^4\left(v_h^2+v_\sigma^2\right)^2} \\
& +\frac{3\log\left(\frac{\left(g_1^2+g_2^2\right)v_h^2}{\mu^2}\right)\left(\left(g_1^2+g_2^2\right)^2v_\sigma^4-2\left(g_1^4+g_2^4\right)v_h^4\right)v_h^4+256g_{B-L}^4v_\sigma^6v_h^2+24M_h^4v_\sigma^2v_h^2+768\log\left(\frac{4g_{B-L}^2v_\sigma^2}{\mu^2}\right)g_{B-L}^4v_\sigma^4\left(2v_h^2-v_\sigma^2\right)v_h^2}{512\pi^2v_h^4\left(v_h^2+v_\sigma^2\right)^2} \\
& +\frac{48\log\left(\frac{M_h^2}{\mu^2}\right)M_h^4\left(2v_h^2-3v_\sigma^2\right)v_h^2-24M_h^4v_\sigma^4+8\log\left(\frac{2M_h^2}{\mu^2}\right)M_h^4\left(-4v_h^4+3v_\sigma^2v_h^2+3v_\sigma^4\right)}{512\pi^2v_h^4\left(v_h^2+v_\sigma^2\right)^2} \\
& +\frac{\log(4)\left(4\left(4v_h^4-3v_\sigma^2v_h^2-3v_\sigma^4\right)M_h^4+3v_h^4\left(\left(10v_h^4+22v_\sigma^2v_h^2-v_\sigma^4\right)g_2^4+8\left(-2v_h^4-4v_\sigma^2v_h^2+v_\sigma^4\right)y_t^4\right)\right)}{512\pi^2v_h^4\left(v_h^2+v_\sigma^2\right)^2},
\end{aligned}
$$

$$
\begin{aligned}
\delta\lambda_{h\sigma} = {} & \frac{8\left(-\log(8)v_h^4+(\log(2)-3)v_\sigma^2v_h^2+3v_\sigma^4\right)M_h^4-24\log\left(\frac{M_h^2}{\mu^2}\right)\left(3v_h^4-4v_\sigma^2v_h^2+3v_\sigma^4\right)M_h^4}{256\pi^2v_h^2v_\sigma^2\left(v_h^2+v_\sigma^2\right)^2} \\
& -\frac{v_h^2v_\sigma^2\left(v_\sigma^2\left(3v_h^2g_1^4+6g_2^2v_h^2g_1^2+48(\log(8)+1)v_h^2y_t^4+15g_2^4v_h^2+256g_{B-L}^4\left(4v_h^2+v_\sigma^2\right)\right)-256\pi^2M_\sigma'^2\left(v_h^2+v_\sigma^2\right)\right)}{256\pi^2v_h^2v_\sigma^2\left(v_h^2+v_\sigma^2\right)^2} \\
& +\frac{v_h^2\left(8\log\left(\frac{2M_h^2}{\mu^2}\right)\left(3v_h^2-v_\sigma^2\right)M_h^4+3v_\sigma^4\left(-12\log\left(\frac{g_2^2v_h^2}{4\mu^2}\right)v_h^2g_2^4+48\log\left(\frac{v_h^2y_t^2}{\mu^2}\right)v_h^2y_t^4-3\log\left(\frac{\left(g_1^2+g_2^2\right)v_h^2}{4\mu^2}\right)\left(g_1^2+g_2^2\right)^2v_h^2\right)\right)}{256\pi^2v_h^2v_\sigma^2\left(v_h^2+v_\sigma^2\right)^2} \\
& +\frac{24v_\sigma^4\left(256\log\left(\frac{4g_{B-L}^2v_\sigma^2}{\mu^2}\right)g_{B-L}^4\left(v_\sigma^2-2v_h^2\right)\right)}{256\pi^2v_h^2v_\sigma^2\left(v_h^2+v_\sigma^2\right)^2}
\end{aligned}
$$

C Full Gravitational Wave Contributions

C.1 Sound waves

The full analytical equation for the sound waves contribution is given below:

$$\begin{aligned}
h^2\Omega_p &= h^2 F_{GW,0} A \left(\frac{\alpha}{1+\alpha}\right)^2 \left(\frac{H_*}{\beta}\right)^2, \\
f_p &\simeq 0.11 H_{*,0} \frac{\beta}{H_*}, \\
f_1 &\simeq 0.2 H_{*,0} (H_* R_*)^{-1}, f_2 \simeq 0.5 H_{*,0} \Delta_\omega^{-1} (H_* R_*)^{-1}, \\
\Delta_\omega &= \frac{\xi_{\rm shell}}{\max(\xi_\omega, c_s)}, \\
h^2\Omega_{\rm int} &= h^2 F_{GW,0} A_{\rm sw} K^2 (H_* \tau_{\rm sw})(H_* R_*), \\
\tau_{\rm sw} &= \min\left(\frac{2H_* R_*}{\sqrt{3K}}, 1\right), \\
K &\simeq \frac{0.6\kappa_{\rm sw}\alpha}{\alpha+1}, \\
\kappa_{\rm sw} &= \frac{\alpha(1-\kappa)^2}{0.73 + 0.083\sqrt{\alpha(1-\kappa)} + \alpha(1-\kappa)}.
\end{aligned} \tag{C.1}$$

$\xi_{\rm shell} = |v_w - c_s|$ is the dimensionless sound shell thickness [10]. From Ref. [58], $A_{\rm sw} \simeq 0.11$.

C.2 MHD Turbulence

The full analytical description of the MHD turbulence contributions are given in Equation C.2.

$$\begin{aligned}
h^2\Omega_{\rm turb} &= 3h^2 A_{\rm MHD}\Omega_s^2 F_{GW,0}(H_*R_*)^3\left(\frac{f}{H_{*,0}}\right)^3 p_\Pi(f, H_*R_*)\mathcal{T}(f,\mathcal{N}H_*\tau_e)\\
\Omega_2 &= F_{GW,0}A_{\rm MHD}\Omega_s^2(H_*R_*)^2\\
\Omega_s &\approx \frac{4}{3}\overline{v}_A^2\\
p_\Pi(f, H_*R_*) &= \left(1+\left(\frac{f}{f_2}\right)^{a_2}\right)^{\frac{-11}{3a_2}}\\
\mathcal{T}(f,\mathcal{N}H_*\tau_e) &= \left(\frac{H_{*,0}}{2\pi f_1}\right)^2\left(1+\left(\frac{f}{f_1}\right)^{a_1}\right)^{\frac{-2}{a_1}}\\
f_1 &\approx \frac{\sqrt{3\Omega_s}}{2\mathcal{N}}\frac{H_{*,0}}{H_*R_*}\\
f_2 &\simeq 2.2\frac{H_{*,0}}{H_*R_*}
\end{aligned} \tag{C.2}$$

From this we can recover a double broken power law, as shown in Equation C.3 [10, 60].

$$\begin{aligned}
h^2\Omega_{\rm turb} &= \Omega_2 \times S_2(f)\\
S_2(f) &= 2^{\frac{11}{3a_2}}\left(\frac{f_1}{f_2}\right)\left(\frac{f}{f_1}\right)^3\left(1+\left(\frac{f}{f_1}\right)^{a_1}\right)^{\frac{-2}{a_1}}\left(1+\left(\frac{f}{f_2}\right)^{a_2}\right)^{\frac{-11}{3a_2}}
\end{aligned} \tag{C.3}$$

The parameters are found to be as follows: $a_1 = 4, a_2 \simeq 2.15, A_{\rm MHD} = 3\cdot\frac{2.2A}{4\pi^2}\cdot 2^{\frac{-11}{3a_2}} \simeq 4.37\cdot 10^{-3}$, and $\mathcal{N} \simeq 2$ [10].

D `TransitionSolver` Results

The results of the `TransitionSolver` code built for Ref. [21] are listed below in Table 3. T_e is the temperature at which the extant volume of false vacuum is $P_f = \frac{1}{e}$, T_f is the temperature at which the transition concluded, and T_γ is the temperature at which the tracing concluded.

Parameter	Numerical result
T_c	29216 GeV
T_n	12322 GeV
T_p	11325 GeV
T_{RH}	15288 GeV
T_e	11240 GeV
T_f	11081 GeV
T_γ	11063 GeV
$S_{3,n}$	127.19 GeV
$S_{3,p}$	116.88 GeV
H_n	$1.7853 \cdot 10^{-10}$ GeV
H_p	$1.6706 \cdot 10^{-10}$ GeV
β_n	$2.4038 \cdot 10^{-8}$ GeV
β_p	$1.8555 \cdot 10^{-8}$ GeV
Mean bubble size	$5.4925 \cdot 10^{7}$ GeV^{-1}
R_p	$2.1254 \cdot 10^{8}$ GeV^{-1}
$v_{w,p}$	0.95836
$\Omega_{\text{sw,peak}}$	$1.7735 \cdot 10^{-10}$
$f_{\text{sw,peak}}$	0.22816 Hz
$\Omega_{\text{turb,peak}}$	$9.4678 \cdot 10^{-13}$
$f_{\text{turb,peak}}$	0.20094 Hz
κ	0.47453
$SNR_{\text{LISA,analytic}}$	0.22911
$SNR_{\text{LISA,PLS}}$	0.46580

Table 3: Numerically determined parameters for the $B - L$ model approximation, as described in Ref. [21] and in Section 3.3.

The results for the $U(1)$ and complex singlet extension, as described in Section 3.3 are given below in Table 4

Parameter	Numerical result
T_c	126.61 GeV
T_n	114.82 GeV
T_p	113.85 GeV
T_{RH}	127.87 GeV
T_e	113.79 GeV
T_f	113.71 GeV
T_γ	113.71 GeV
$S_{3,n}$	142.73 GeV
$S_{3,p}$	123.19 GeV
H_n	$1.5746 \cdot 10^{-14}$ GeV
H_p	$1.5527 \cdot 10^{-14}$ GeV
β_n	$4.1065 \cdot 10^{-11}$ GeV
β_p	$3.1870 \cdot 10^{-11}$ GeV
Mean bubble size	$2.7613 \cdot 10^{10}$ GeV^{-1}
R_p	$9.5905 \cdot 10^{10}$ GeV^{-1}
$v_{w,p}$	0.80052
$\Omega_{\text{sw,peak}}$	$7.1306 \cdot 10^{-15}$
$f_{\text{sw,peak}}$	0.076868 Hz
$\Omega_{\text{turb,peak}}$	$3.3422 \cdot 10^{-17}$
$f_{\text{turb,peak}}$	0.044050 Hz
κ	0.039747
$SNR_{\text{LISA,analytic}}$	0.00061716
$SNR_{\text{LISA,PLS}}$	0.0026537

Table 4: Numerically determined parameters obtained using `TransitionSolver` for the $U(1)$ and complex singlet extension, as described in Section 3.3.

The graphs obtained from `TransitionSolver` for the $B-L$ and complex singlet extension are listed below as Figures 10 and 11, and Figures 12 and 13 respectively.

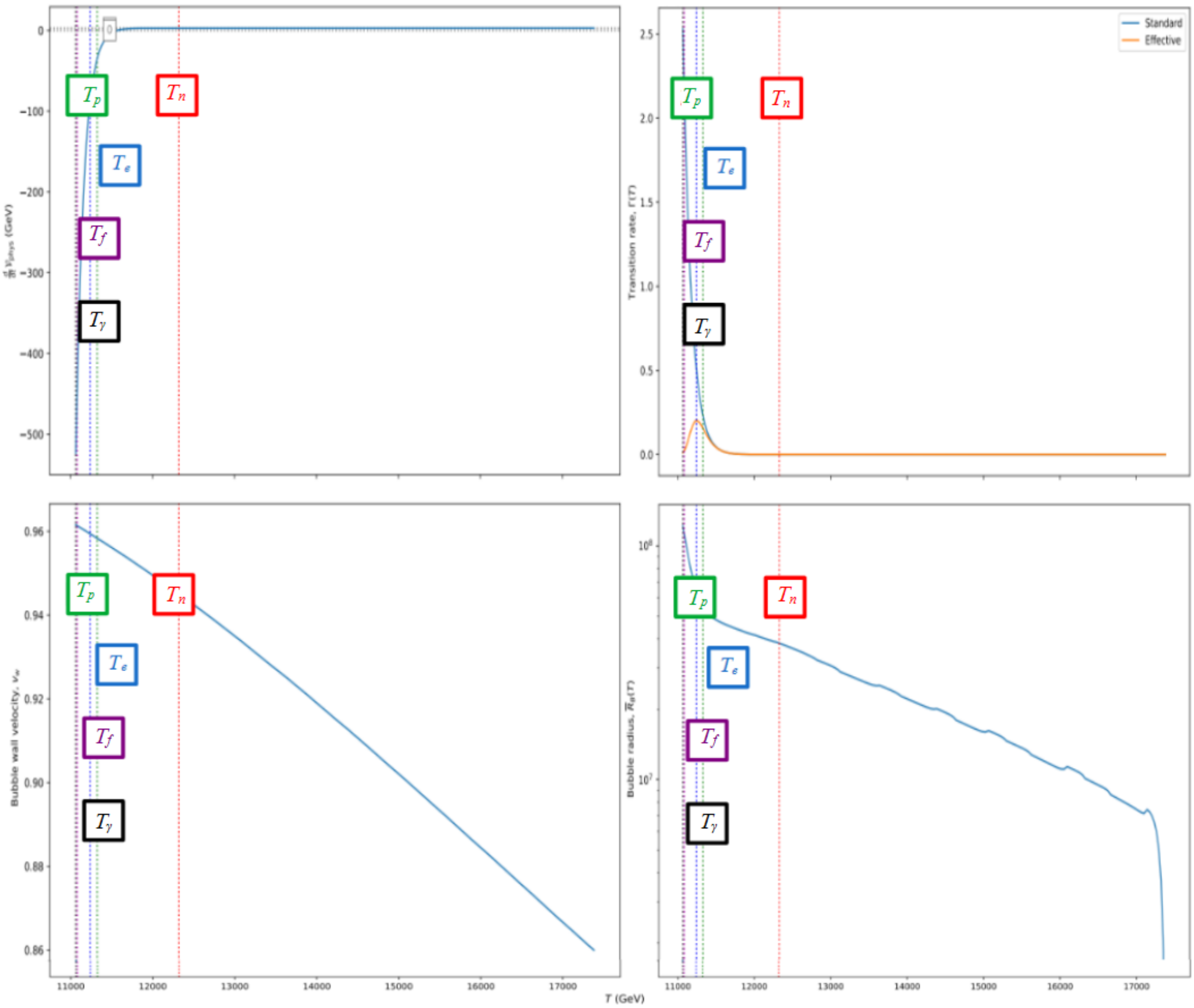

Figure 10: Temperature evolution of the relevant transition quantities in the simplified $B-L$ benchmark , with T_n, T_p,T_e, T_f and T_γ marked.

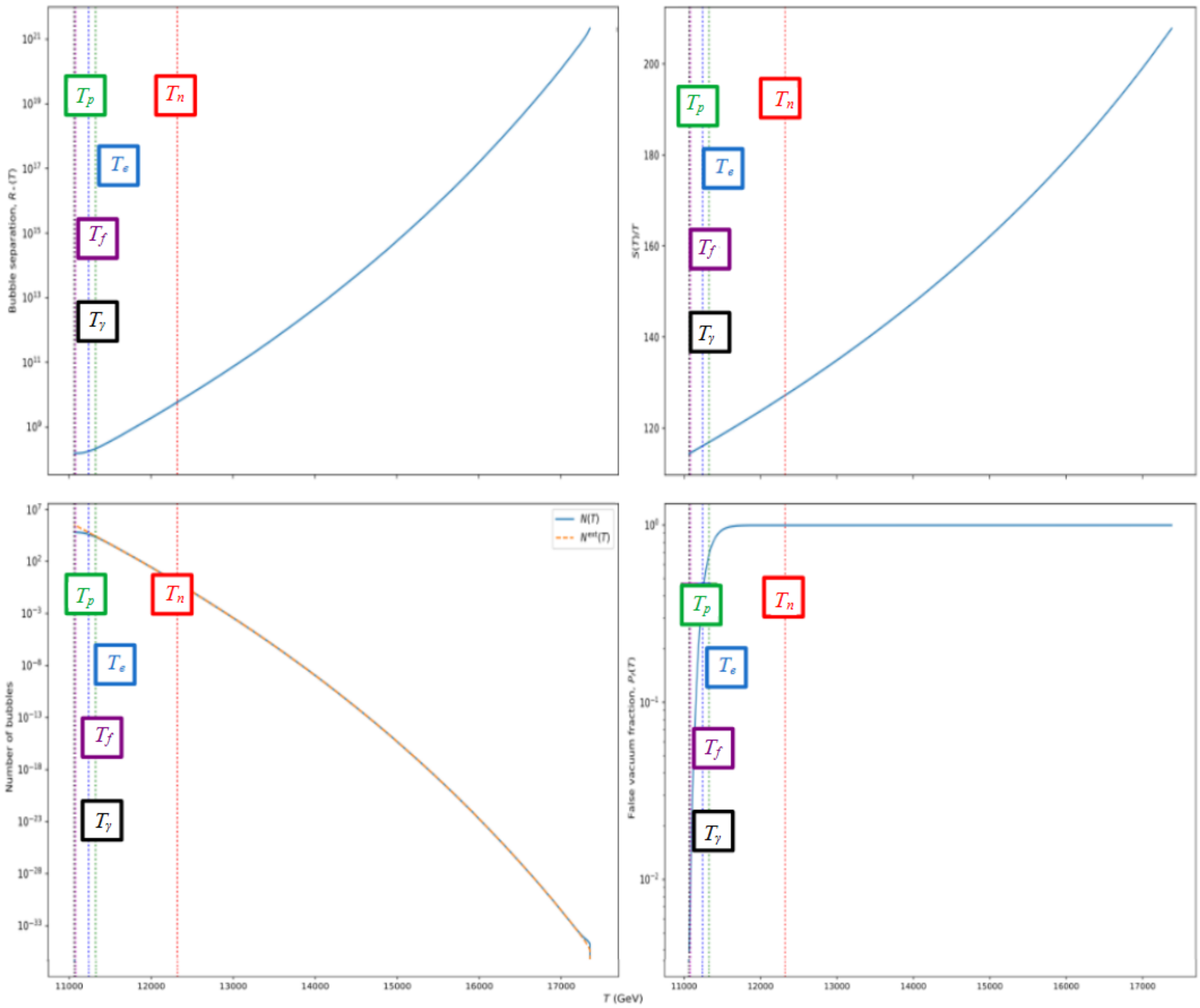

Figure 11: Temperature evolution of the relevant transition quantities in the simplified $B-L$ benchmark , with T_n, T_p,T_e, T_f and T_γ marked.

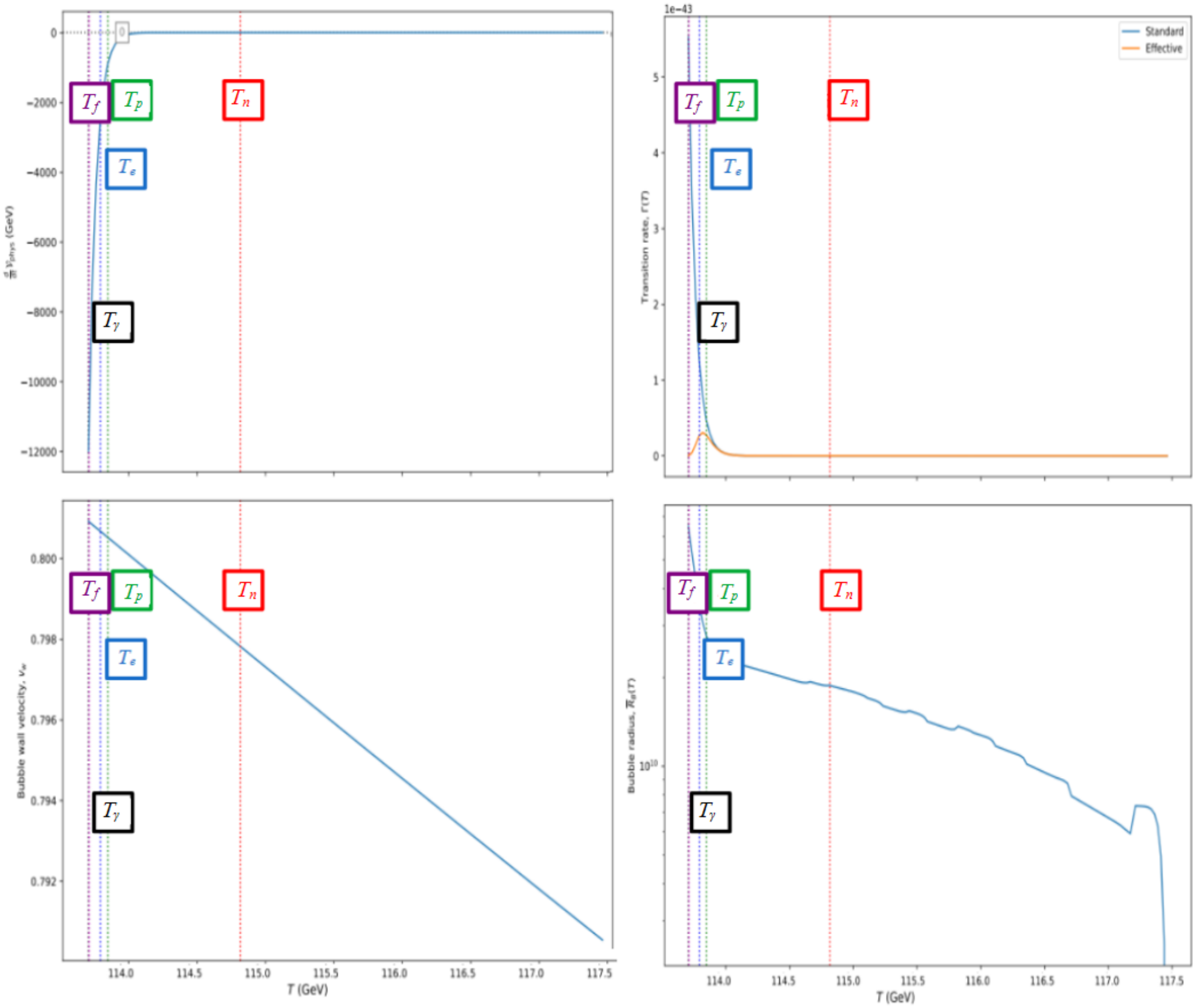

Figure 12: Temperature evolution of relevant transition quantities in the $U(1)$+complex-singlet proxy benchmark, with T_n, T_p, T_e, T_f and T_γ marked.

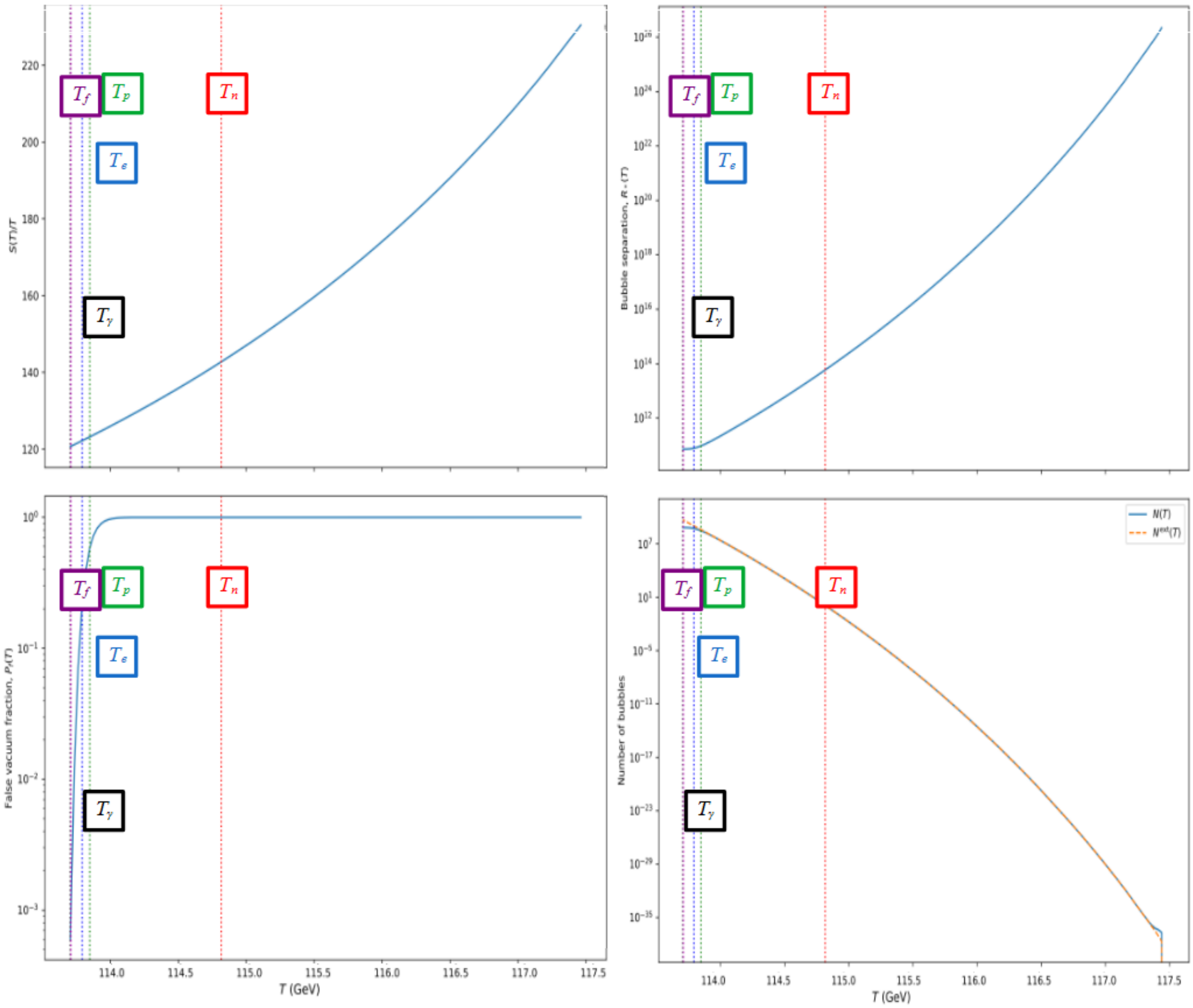

Figure 13: Temperature evolution of relevant transition quantities in the $U(1)$+complex-singlet proxy benchmark, with T_n, T_p, T_e, T_f and T_γ marked.

Additional scans for the proxy model are shown in Figures 14 and 15. They illustrate benchmark-level trends with v_σ, $M_{Z'}$, peak frequency and peak amplitude. Because the scan is sparse, these trends should not be interpreted as a statistically robust parameter-space result.

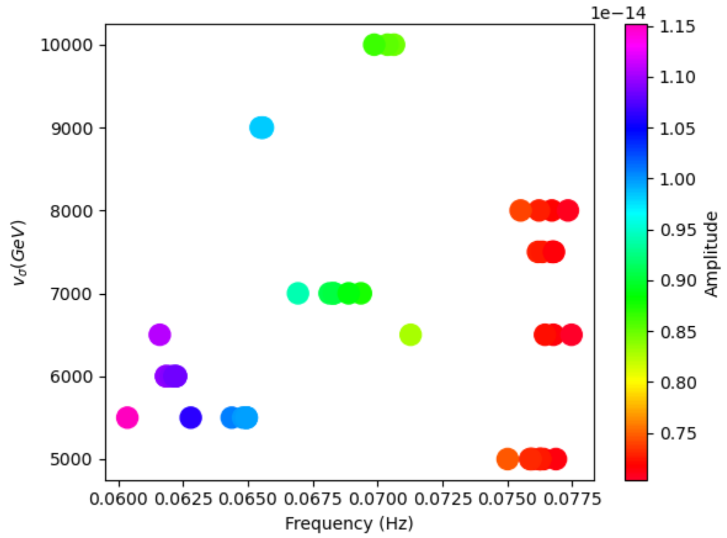

Figure 14: Peak frequency and amplitude as functions of v_σ for the scanned proxy-model benchmark points.

Figure 15 shows the relation between peak frequency and peak amplitude, with the colour scale indicating $\log(M_{Z'})$.

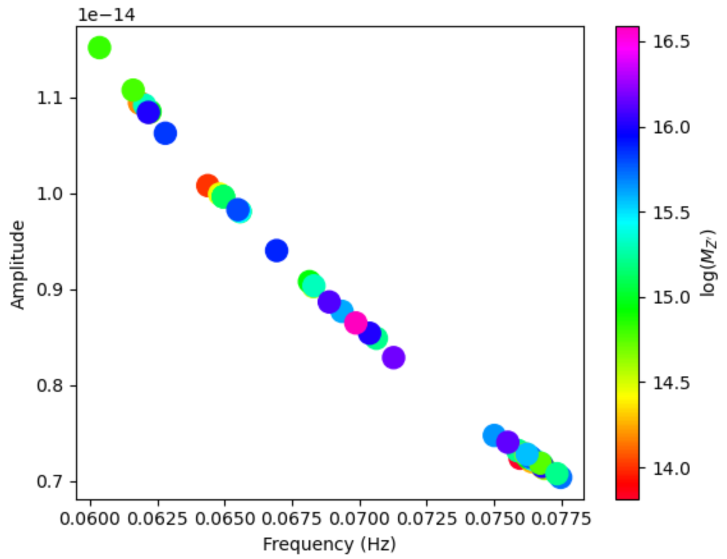

Figure 15: Relation between peak amplitude and peak frequency for the scanned proxy-model benchmark points, with the colour scale indicating $\log(M_{Z'})$.

References

[1] *LIGO Scientific*, *Virgo Cooperation*, "Observation of gravitational waves from a binary black hole merger", Physical Review Letters **116**, 10.1103/physrevlett.116.061102 (2016).

[2] P. Athron et al., "Cosmological phase transitions: from perturbative particle physics to gravitational waves", Progress in Particle and Nuclear Physics **135**, 104094 (2024).

[3] Y. Cheng, S.-F. Ge, J. Sheng, and T. T. Yanagida, "Right-handed neutrino dark matter with forbidden annihilation", Physical Review D **107**, 10.1103/physrevd.107.123013 (2023).

[4] P. Cox, C. Han, and T. T. Yanagida, "Right-handed neutrino dark matter in a u(1) extension of the standard model", Journal of Cosmology and Astroparticle Physics **2018**, 029 (2018).

[5] S. Hawking and I. Moss, "Supercooled phase transitions in the very early universe", Physics Letters B **110**, 35–38 (1982).

[6] A. D. Sakharov, "Violation of cp invariance, c asymmetry, and baryon asymmetry of the universe", Pisma Zh. Eksp. Teor. Fiz. **5**, 32–35 (1967).

[7] C. Marzo, L. Marzola, and V. Vaskonen, "Phase transition and vacuum stability in the classically conformal b–l model", The European Physical Journal C **79**, 10.1140/epjc/s10052-019-7076-x (2019).

[8] J. Gonçalves, D. Marfatia, A. P. Morais, and R. Pasechnik, "Gravitational waves from supercooled phase transitions in conformal majoron models of neutrino mass", Journal of High Energy Physics **2025**, 10.1007/jhep02(2025)110 (2025).

[9] A. Kobakhidze, C. Lagger, A. Manning, and J. Yue, "Gravitational waves from a supercooled electroweak phase transition and their detection with pulsar timing arrays", The European Physical Journal C **77**, 10.1140/epjc/s10052-017-5132-y (2017).

[10] C. Caprini et al., "Gravitational waves from first-order phase transitions in lisa: reconstruction pipeline and physics interpretation", Journal of Cosmology and Astroparticle Physics **2024**, 020 (2024).

[11] J. Gonçalves, D. Marfatia, A. P. Morais, and R. Pasechnik, "Supercooled phase transitions in conformal dark sectors explain nanograv data", Physics Letters B **869**, 139829 (2025).

[12] NANOGrav Collaboration, G. Agazie, et al., "The nanograv 15 yr data set: evidence for a gravitational-wave background", The Astrophysical Journal Letters **951**, L8 (2023).

[13] PPTA Collaboration, A. Zic, et al., "The parkes pulsar timing array third data release", Publications of the Astronomical Society of Australia **40**, 10.1017/pasa.2023.36 (2023).

[14] EPTA Collaboration, Antoniadis, J., et al., "The second data release from the european pulsar timing array - i. the dataset and timing analysis", A&A **678**, A48 (2023).

[15]C. Caprini et al. (LISA Science), "Science of the LISA mission: A Summary for the European Strategy for Particle Physics", (2025).

[16]C. Caprini et al., "Reconstructing the spectral shape of a stochastic gravitational wave background with lisa", Journal of Cosmology and Astroparticle Physics **2019**, 017–017 (2019).

[17]M. K. Gaillard, P. D. Grannis, and F. J. Sciulli, "The standard model of particle physics", Reviews of Modern Physics **71**, S96–S111 (1999).

[18]J. P. Garcés, F. Goertz, M. Lindner, and Á. Pastor-Gutiérrez, "The quantum criticality of the standard model and the hierarchy problem", Journal of High Energy Physics **2025** (2025).

[19]S. Oda, N. Okada, and D.-s. Takahashi, "Classically conformal u(1)' extended standard model and higgs vacuum stability", Physical Review D **92**, `10.1103/physrevd.92.015026` (2015).

[20]S. Iso, N. Okada, and Y. Orikasa, "Classically conformal b–l extended standard model", Physics Letters B **676**, 81–87 (2009).

[21]P. Athron, S. Datta, and Z.-Y. Zhang, *Probing thermal leptogenesis and dark matter through primordial gravitational waves from a supercooled universe*, 2025.

[22]S. Khalil, "TeV-scale gauged B-L symmetry with inverse seesaw mechanism", Phys. Rev. D **82**, 077702 (2010).

[23]X.-X. Dong et al., "Gravitational waves from the phase transition in the b-lssm", Journal of High Energy Physics (2021).

[24]N. Haba and T. Yamada, "Gravitational waves from phase transition in minimal susy u(1)b-l model", Physical Review D **101** (2020).

[25]A. Ahriche, S. Kanemura, and M. Tanaka, "Gravitational waves from phase transitions in scale invariant models", JHEP **01**, 201 (2024).

[26]P. Arnold and O. Espinosa, "Effective potential and first-order phase transitions: beyond leading order", Phys. Rev. D **47**, 3546–3579 (1993).

[27]P. Athron, C. Balazs, A. Fowlie, and Y. Zhang, "PhaseTracer: tracing cosmological phases and calculating transition properties", Eur. Phys. J. C **80**, 567 (2020).

[28]P. Athron et al., "PhaseTracer2: from the effective potential to gravitational waves", Eur. Phys. J. C **85**, 559 (2025).

[29]P. Athron, C. Balázs, and L. Morris, "Supercool subtleties of cosmological phase transitions", JCAP **03**, 006 (2023).

[30]E. Bertuzzo, C. Csaki, and F. Huller, "Electroweak precision constraints on dark photon models with generalized mixing", Journal of High Energy Physics **2026**, `10.1007/jhep03(2026)155` (2026).

[31]E. Gildener and S. Weinberg, "Symmetry breaking and scalar bosons", Phys. Rev. D **13**, 3333–3341 (1976).

[32]S. Coleman and E. Weinberg, "Radiative corrections as the origin of spontaneous symmetry breaking", Phys. Rev. D **7**, 1888–1910 (1973).

[33]P. Basler and M. Mühlleitner, "Bsmpt (beyond the standard model phase transitions): a tool for the electroweak phase transition in extended higgs sectors", Computer Physics Communications **237**, 62–85 (2019).

[34]Gustavsson, Filip, *Cosmological Signatures of the Scale-Invariant Two-Higgs-Doublet Model with an Additional Scalar Singlet*, eng, Student Paper, 2025.

[35]Holmström, Hjalmar, *On-Shell Renormalization of the General 2HDM*, eng, Student Paper, 2025.

[36]D. Curtin, P. Meade, and H. Ramani, *Thermal resummation and phase transitions*, 2016.

[37]J. Espinosa, M. Quirós, and F. Zwirner, "On the nature of the electroweak phase transition", Physics Letters B **314**, 206–216 (1993).

[38]J. Li and P. Nath, *Gravitational waves from supercooled phase transitions and pulsar timing array signals*, Proceedings of the Corfu Summer Institute 2025, BSM 2025 Conference, Feb. 2026.

[39]A. D. Linde, "Decay of the false vacuum at finite temperature: a. linde, nucl. phys. b216 (1983) 421", Nuclear Physics B **223**, 544 (1983).

[40]S. R. Coleman, "The Fate of the False Vacuum. 1. Semiclassical Theory", Phys. Rev. D **15**, [Erratum: Phys.Rev.D 16, 1248 (1977)], 2929–2936 (1977).

[41]J. Ellis, M. Lewicki, and J. M. No, "On the maximal strength of a first-order electroweak phase transition and its gravitational wave signal", Journal of Cosmology and Astroparticle Physics **2019**, 003–003 (2019).

[42]L. Husdal, "On effective degrees of freedom in the early universe", Galaxies **4**, 78 (2016).

[43]R.-G. Cai, M. Sasaki, and S.-J. Wang, "The gravitational waves from the first-order phase transition with a dimension-six operator", Journal of Cosmology and Astroparticle Physics **2017**, 004–004 (2017).

[44]J. Ellis, M. Lewicki, J. M. No, and V. Vaskonen, "Gravitational wave energy budget in strongly supercooled phase transitions", Journal of Cosmology and Astroparticle Physics **2019**, 024–024 (2019).

[45]C. Caprini et al., "Detecting gravitational waves from cosmological phase transitions with lisa: an update", Journal of Cosmology and Astroparticle Physics **2020**, 024–024 (2020).

[46]A. Mégevand and S. Ramírez, "Bubble nucleation and growth in very strong cosmological phase transitions", Nuclear Physics B **919**, 74–109 (2017).

[47]C. Caprini et al., "Science with the space-based interferometer elisa. ii: gravitational waves from cosmological phase transitions", Journal of Cosmology and Astroparticle Physics **2016**, 001–001 (2016).

[48]C. Caprini and R. Durrer, “Gravitational waves from stochastic relativistic sources: primordial turbulence and magnetic fields”, Physical Review D **74**, 10.1103/physrevd.74.063521 (2006).

[49]P. Binétruy, A. Bohé, C. Caprini, and J.-F. Dufaux, “Cosmological backgrounds of gravitational waves and elisa/ngo: phase transitions, cosmic strings and other sources”, Journal of Cosmology and Astroparticle Physics **2012**, 027–027 (2012).

[50]M. Kamionkowski, A. Kosowsky, and M. S. Turner, “Gravitational radiation from first-order phase transitions”, Physical Review D **49**, 2837–2851 (1994).

[51]S. J. Huber and T. Konstandin, “Gravitational wave production by collisions: more bubbles”, Journal of Cosmology and Astroparticle Physics **2008**, 022 (2008).

[52]A. Mégevand and F. A. Membiela, “Gravitational waves from bubble walls”, Journal of Cosmology and Astroparticle Physics **2021**, 073 (2021).

[53]A. Kosowsky and M. S. Turner, “Gravitational radiation from colliding vacuum bubbles: envelope approximation to many-bubble collisions”, Physical Review D **47**, 4372–4391 (1993).

[54]M. Lewicki and V. Vaskonen, “Gravitational waves from colliding vacuum bubbles in gauge theories”, The European Physical Journal C **81**, 10.1140/epjc/s10052-021-09232-3 (2021).

[55]M. Lewicki and V. Vaskonen, “Gravitational waves from bubble collisions and fluid motion in strongly supercooled phase transitions”, The European Physical Journal C **83**, 10.1140/epjc/s10052-023-11241-3 (2023).

[56]M. Hindmarsh, “Sound shell model for acoustic gravitational wave production at a first-order phase transition in the early universe”, Physical Review Letters **120**, 10.1103/physrevlett.120.071301 (2018).

[57]M. Hindmarsh and M. Hijazi, “Gravitational waves from first order cosmological phase transitions in the sound shell model”, Journal of Cosmology and Astroparticle Physics **2019**, 062–062 (2019).

[58]R. Jinno, T. Konstandin, H. Rubira, and I. Stomberg, “Higgsless simulations of cosmological phase transitions and gravitational waves”, Journal of Cosmology and Astroparticle Physics **2023**, 011 (2023).

[59]J. Ellis, M. Lewicki, and V. Vaskonen, “Updated predictions for gravitational waves produced in a strongly supercooled phase transition”, Journal of Cosmology and Astroparticle Physics **2020**, 020–020 (2020).

[60]A. R. Pol et al., *Lisa and γ-ray telescopes as multi-messenger probes of a first-order cosmological phase transition*, 2026.

[61]R. Banerjee and K. Jedamzik, “Evolution of cosmic magnetic fields: from the very early universe, to recombination, to the present”, Physical Review D **70**, 10.1103/physrevd.70.123003 (2004).

[62]M. Laine, “Bubble growth as a detonation”, Physical Review D **49**, 3847–3853 (1994).

[63]ATLAS Collaboration, G. Aad, et al., “Search for $t\bar{t}$ resonances in fully hadronic final states in pp collisions at $\sqrt{s} = 13$ tev with the atlas detector”, Journal of High Energy Physics **2020**, `10.1007/jhep10(2020)061` (2020).

[64]ATLAS Collaboration, G. Aad, et al., “Search for high-mass dilepton resonances using 139 fb-1 of pp collision data collected at $\sqrt{s} = 13$ tev with the atlas detector”, Physics Letters B **796**, 68–87 (2019).

[65]ATLAS Collaboration, M. Aaboud, et al., “Search for additional heavy neutral higgs and gauge bosons in the ditau final state produced in 36 fb-1 of pp collisions at $\sqrt{s} = 13$ tev with the atlas detector”, Journal of High Energy Physics **2018**, `10.1007/jhep01(2018)055` (2018).